Master Thesis

The influence of donor-to-donor migration on luminescence

Author:
Jarich Haitjema

Supervisors:
Mathijs de Jong, Freddy Rabouw and Andries Meijerink

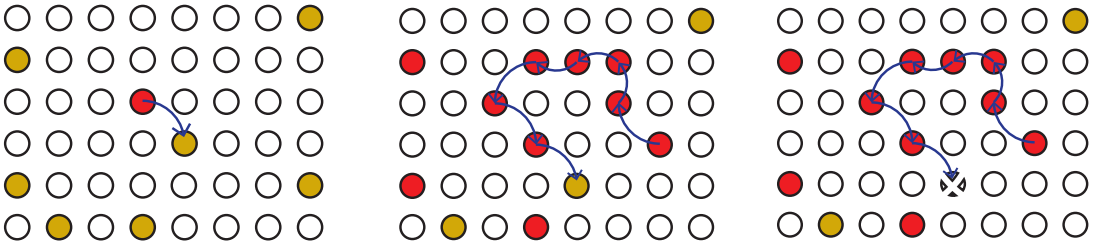

Condensed Matter and Interfaces
Debye Institute for Nanomaterials Science
Utrecht University

August 5, 2015

Abstract

Förster energy transfer is an important mechanism that enables spectral conversion materials to use two types of luminescent centres: one optimized for strong absorption, and one efficiently emitting the desired color of light. Additionally, it lies at the core of upconversion and downconversion processes which are promising for increasing the efficiency of solar cells. Due to lack of a good model, the optimum concentration of dopants for upconversion or downconversion materials is not known. It can be desirable to have a high doping concentration of donor ions, because that leads to strong light absorption. At such high doping concentrations donor-to-donor energy migration can start to play a role, affecting the luminescence both in positive and negative ways. This process is highly relevant in luminescent phosphors as well as in luminescent quantum dots and biomolecular systems with dyes. The process is often poorly understood, demanding a thorough study using a simple, well-defined system. Therefore, we quantified the effects of this migration on the luminescence properties of the crystalline systems $LaPO_4$: Ce^{3+}, Nd^{3+} and YPO_4: Gd^{3+}, Er^{3+}, where Ce^{3+} and Gd^{3+} were used as donor ions and Nd^{3+} and Er^{3+} as acceptor ions. First, the lifetime of the donor ion luminescence and the donor-acceptor transfer strength were measured using luminescence decay curves of samples with a low donor concentration. At low donor concentrations, analytical fitting procedures which neglect migration can be used to obtain the lifetime and donor-acceptor strength. The lifetimes of Ce^{3+} and Gd^{3+} were measured to be 16.66 ns and 4.454 ms, respectively. The donor-to-acceptor transfer strength, a constant which is independent of the distance between the ions, was measured to be around 0.0025 $ns^{-1}Å^6$ for Ce^{3+}–Nd^{3+} transfer and around 0.0022 $ms^{-1}Å^6$ for Gd^{3+}–Er^{3+} transfer. Monte Carlo simulations which include migration were then used to simulate luminescence decay in a crystal doped with luminescent ions, placing these ions on random positions of the lattice and calculating the theoretical luminescence decay curves, using the experimentally obtained lifetimes and donor-to-acceptor-strengths. The decay was compared to experimental luminescence decay curves of samples with a high concentration of donors. The donor-to-donor migration strength in the model was varied in order to obtain the best possible agreement with the experimental data. We conclude that the Ce^{3+}–Ce^{3+} migration strength is of the same order of magnitude as the Ce^{3+}–Nd^{3+} transfer rate, and that the Gd^{3+}–Gd^{3+} migration strength is one order of magnitude higher than the Gd^{3+}–Er^{3+} strength. The characteristic Förster radii, the distances at which energy migration is equally probable as the radiative decay, were estimated to be 0.49 nm for Ce^{3+}–Ce^{3+} and 0.67 nm for Gd^{3+}–Gd^{3+}.

Contents

Chapter 1

Introduction

Luminescent phosphors form an important class of materials that are widely used in fluorescent light bulbs, as well as in television screens and fluorescent bio-imaging. The main mechanism that is utilized for light conversion processes in these phosphors is Förster resonance energy transfer (FRET). In the process, a luminescent center referred to as the "donor" is excited by incoming light, after which energy transfer takes place to another luminescent center referred to as the "acceptor". The rate at which this process occurs is strongly dependent on the donor-acceptor distance: the rate decays with the distance to the power of six. This distance dependence was discovered in 1948 by Th. Förster [1], and is further discussed in the theory section (Chapter 2).

An exciting new discovery in the field of phosphors is the existence of upconverting and downconverting phosphors [2] [3]. Upconversion denotes a process in which two or more lower-energy photons are converted to one higher energy photon. Downconversion is the opposite process, in which one higher-energy photon is converted to two or more lower-energy photons. FRET is one of the mechanisms that is responsible for both up- and downconversion.

Upconversion and downconversion are processes that are promising for increasing the efficiency of solar cells [4]. The solar spectrum consists of a broad band over a large wavelength range (see Fig. 1.1) while the band gap of Si is located at about 1.11 eV. Photons with a lower energy cannot be absorbed by Si while the excess energy of photons with a higher energy is lost following absorption.

Upconversion and downconversion can help alleviate these losses by converting photons to the desired energy of 1.11 eV. For these processes, a high concentration of dopants is often required to increase absorption of incoming light [2]. At such high concentrations, *migration* of the excitation energy among luminescent centers can occur, affecting the luminescence both in positive and negative ways [6]. On one hand migration can lead to subsequent transfer to an acceptor center. On the other hand, migration can also lead to subsequent transfer to a defect in the lattice after which the excitation energy is lost non-radiatively [7]. These processes are depicted in figure 1.2. It is clear that the migration process can affect the luminescence in different ways and that the effect is by no means trivial.

Therefore, in the 60s and 70s some attempts were made to investigate this donor-to-donor migration by studying luminescence decay curves. For instance, in 1967 Yokota and Tanimoto tried to approximate donor-to-donor migration by regarding it as a diffusion process [8]. In 1984, Burshtein published a review paper considering different approaches to study energy transfer kinetics in disordered systems [9]. However, all these approaches utilize a completely random distribution of

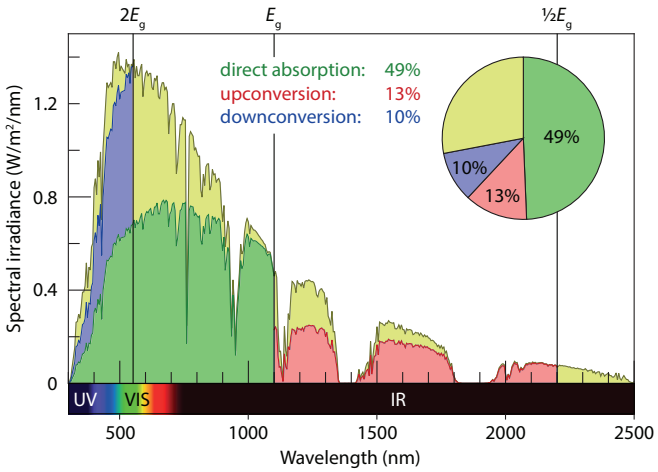

Figure 1.1: The AM1.5D solar spectrum (yellow). The silicon band gap is located around 1130 nm; photons with a longer wavelength are not absorbed and photons with a shorter wavelength are absorbed with loss of energy. The image shows that 49% of solar power can be directly absorbed by Si (green), while 13% of solar power can be utilized through 2-to-1 upconversion (red) and 10% of the spectrum by 1-to-2 downconversion (blue). Image taken from Ref. [5].

luminescent centers, where all donor-donor and donor-acceptor distances are possible. This might be an acceptable approach to describe the behavior of luminescent biomolecules in solution, but in a crystalline environment, where ions are arranged in a highly ordered microscopic structure, this approach is doomed to fail. More recently, Carlsson tried a new approach to donor-to-donor migration to study fluorescence depolarization of organic molecules [10]. This approach was later used to design 'photonic wires': DNA strands with intercalated dye molecules which can migrate excitation energy over very long distances [11] (see Fig. 1.3).

Monte Carlo simulations were used to randomly place dyes on discrete positions near the DNA strands. This is an interesting approach because only discrete positions on the DNA strands are allowed, a similar situation to luminescent ions in crystals. Moreover, this approach underlines the high relevance of donor-to-donor migration in biomolecular systems, despite the fact that it is often still poorly understood [6]. Because biomolecular systems are often complicated, using a simpler and better defined system such as a crystal to study donor-to-donor migration is very promising.

The group of Condensed Matter and Interfaces in Utrecht is interested in luminescence of rare earth ions, and investigates their luminescent behavior by synthesizing the luminescent materials and performing luminescence measurements and computer simulations. Investigating up- and downconversion and the fundamental processes that lie behind it is one of the aims of the group [2] [3]. In the group, synthesis of nanocrystals doped with luminescent rare earth ions and measurements on these materials is also performed [12]. Donor-to-donor migration can be very relevant in these systems as well.

The aim of this work is to contribute to this research by studying the effect that the migration process has on luminescence properties. Two different systems were chosen to study energy migration: $LaPO_4$: Ce^{3+}, Nd^{3+} and YPO_4: Gd^{3+}, Er^{3+}.

The ultimate goal is to be able to predict the effect of energy migration for any model system,

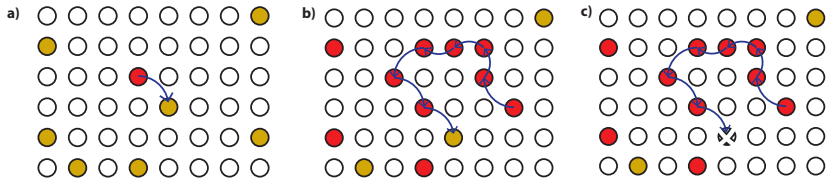

Figure 1.2: We have a crystal that is partially occupied with donor (red) and acceptor (yellow) ions. The luminescent donors are excited using a laser pulse. **a)** Simple donor-to-acceptor transfer from a donor to an acceptor **b)** Donor-to-donor migration with subsequent transfer to an acceptor center and **c)** Donor-to-donor migration with subsequent transfer to a defect in the crystal after which the excitation energy is lost non-radiatively.

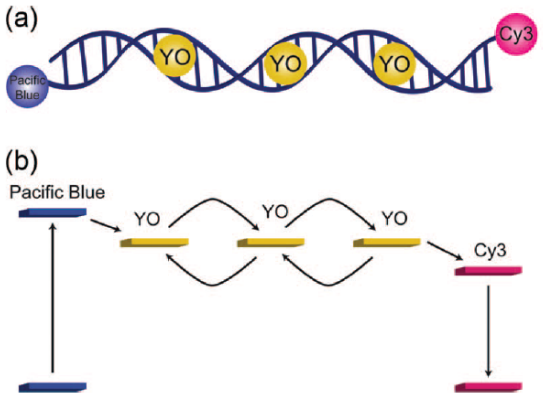

Figure 1.3: A DNA 'photonic wire' in which a Pacific Blue dye molecule absorbs blue light. The excitation energy travels via donor-to-donor migration over various oxazole yellow (YO) molecules, after which an acceptor (Cytochrome dye molecule) that emits red light is reached. Image taken from Ref. [11].

based on a few elementary parameters of the system (e.g. crystal structure and type of luminescent ions). If this effect can be predicted, an optimum donor and acceptor concentration for the application can be calculated.

Chapter 2

Theory

2.1 Lanthanides

Lanthanides form a group of elements with an atomic number increasing from 57 (lanthanum) to 71 (lutetium). The most common valency among lanthanides is +3, resulting in an electron configuration of [Xe]$4f^n$. Extra electrons added to the $4f$ orbital are strongly shielded by the $5s$ and $5p$ orbitals and do not significantly affect the chemical environment. For this reason, the lanthanides are chemically very similar.

Lanthanides are very useful in emerging new technologies due to their interesting optical and magnetic properties. They are used in opto-electronic devices such as smart phones, tablets etc. as well as in medical applications (MRI, PET scans). Although the lanthanides are chemically similar, there are still some chemical differences. Going from lighter lanthanides to heavier lanthanides, the radii of the trivalent lanthanide ions decrease; this is referred to as the lanthanide contraction [13]. Because there are extra protons present in the nucleus of heavier lanthanides, the effective charge of the atom experienced by the outer shell electrons increases. This increased charge is poorly shielded by the extra $4f$ electrons, resulting in the outer shell being drawn towards the nucleus.

The element yttrium (Y) is located above lanthanum in the periodic table and is therefore chemically similar to lanthanum, with a most common oxidation state of +3. Due to the smaller ion radius, it is most similar to the heavier lanthanides. The element yttrium is classified under the rare earths (RE), a group of metals which consists of the fifteen lanthanides plus scandium (Sc) and yttrium. Although the Y^{3+} ion has no f-electrons and therefore less interesting optical properties, it is often used in luminescent phosphors because it can provide a crystal lattice in which other rare earth ions can be incorporated [14].

Despite the chemical similarity, optical properties of lanthanides can differ strongly. The n electrons can be distributed in $\binom{14}{n}$ different ways over the $4f$ shell, which has seven different orbitals. Not all of these configurations have the same energy. If there is more than one electron in the $4f$ shell, the electrons will experience a Coulombic electron-electron repulsion. This Coulombic repulsion is not the same for each configuration because the $4f$ orbitals have different shapes.

Additionally, there is an interaction between the electrons due to coupling of the magnetic field generated by their spin or orbital motion, which can also be different for each configuration. The energy configurations are described by term symbols. In addition, these term symbols are further split by the crystal field of the chemical environment. This effect is rather small for lanthanides due to strong shielding of the $4f$ orbitals and we will not consider it further.

2.1.1 Term symbols

The possible configurations in a $4f$ shell can be characterized as follows [13]. Firstly, we have to know the *quantum numbers* of each different electron. There are four different quantum numbers: the principal, azimuthal, magnetic and spin projection quantum numbers. Pauli's exclusion principle states that no two electrons may possess the same set of quantum numbers. The principle quantum number n describes the electron shell and is the same (namely, 4) for all electrons in the $4f$ shell. The azimuthal quantum number l describes the subshell and also gives the magnitude of the orbital angular momentum. Additionally, it determines which values of the magnetic quantum number m_l are possible. If the azimuthal quantum number has a value of l, the magnetic quantum number has $2l+1$ possible values: $l, (l-1), ...0, ..., -l$. The $4f$ electrons in lanthanides have $l = 3$ so that $m_l = -3, ...0, ..., 3$. Finally, we have the spin projection quantum number m_s which describes the spin of an electron within an orbital. Similarly to the magnetic quantum number, it can assume values of $s, (s-1), ..., 0..., -(s-1)$, where s is the spin quantum number. For electrons, the spin quantum number $s = 1/2$, so that m_s can assume values of $\pm 1/2$.

Now we move on from a single electron to an ensemble of electrons. The resultant orbital angular momentum L of a multi-electron species is related to the values of l for the individual electrons. Since the orbital angular momentum has magnitude and direction, vectorial summation of individual l values is necessary. The allowed values of L can be determined from l for the individual electrons in the multi-electron system. For two electrons with values of l_1 and l_2:

$$L = (l_1 + l_2), (l_1 + l_2 - 1), \ ... \ |l_1 - l_2| \tag{2.1}$$

Energy states for which $L = 0, 1, 2, 3, 4...$ are known as S, P, D, F, G... terms, respectively.

We can perform a similar procedure to obtain possible values for the resultant spin quantum number S. For a system with n electrons, each having $s = 1/2$, possible values of S fall into two series depending on the total number of electrons: for an odd number of electrons S can assume values of $1/2$, $3/2$, $5/2$, ... while for an even number of electrons it can assume values of 1, 2, 3, ...

To properly account for interaction between the total orbital angular momentum and total spin angular momentum (spin-orbit coupling) we need to introduce another quantum number, J. This quantum number also allows vector addition, so possible values are $|L-S|, ..., |L+S|$. For example, in the ground state of the Ce^{3+} ion, $L = 3$ and $S = 1/2$. J can therefore take the values of $5/2$ and $7/2$.

The energy levels are characterized by the term symbol ${}^{2S+1}L_J$, in which L is the sum of all magnetic quantum numbers m_l of the electrons and S is the sum of all spin quantum numbers m_s. For example, the ion Ce^{3+} would have a ${}^2F_{7/2}$ and ${}^2F_{5/2}$ term in the $4f^1$ configuration.

2.1.2 $f - f$ transitions

In Fig. 2.1 the most common energy states present in trivalent lanthanide ions are listed. Transitions from the ground state to different electron configurations can take place, for example by excitation due to incident light. Because these $f - f$ transitions are parity forbidden, the absorption coefficient is usually low for these transitions ($\epsilon_{\max}$ = 10–100 M^{-1} cm^{-1}) and luminescence lifetimes of excited f states are usually long, on the order of a few ms. The emission and excitation peaks are typically quite sharp, because the offset between the parabolas that describe the $4f$ states in a configurational coordinate diagram [15] is small. The crystal field splitting of the excited f states is also small, which opens up the possibility to create a diagram of all possible $4f^n$ levels, which is valid for Ln^{3+} ions in any material. This was done by G.H. Dieke in 1968, and the diagram is therefore referred to as the "Dieke diagram" [16].

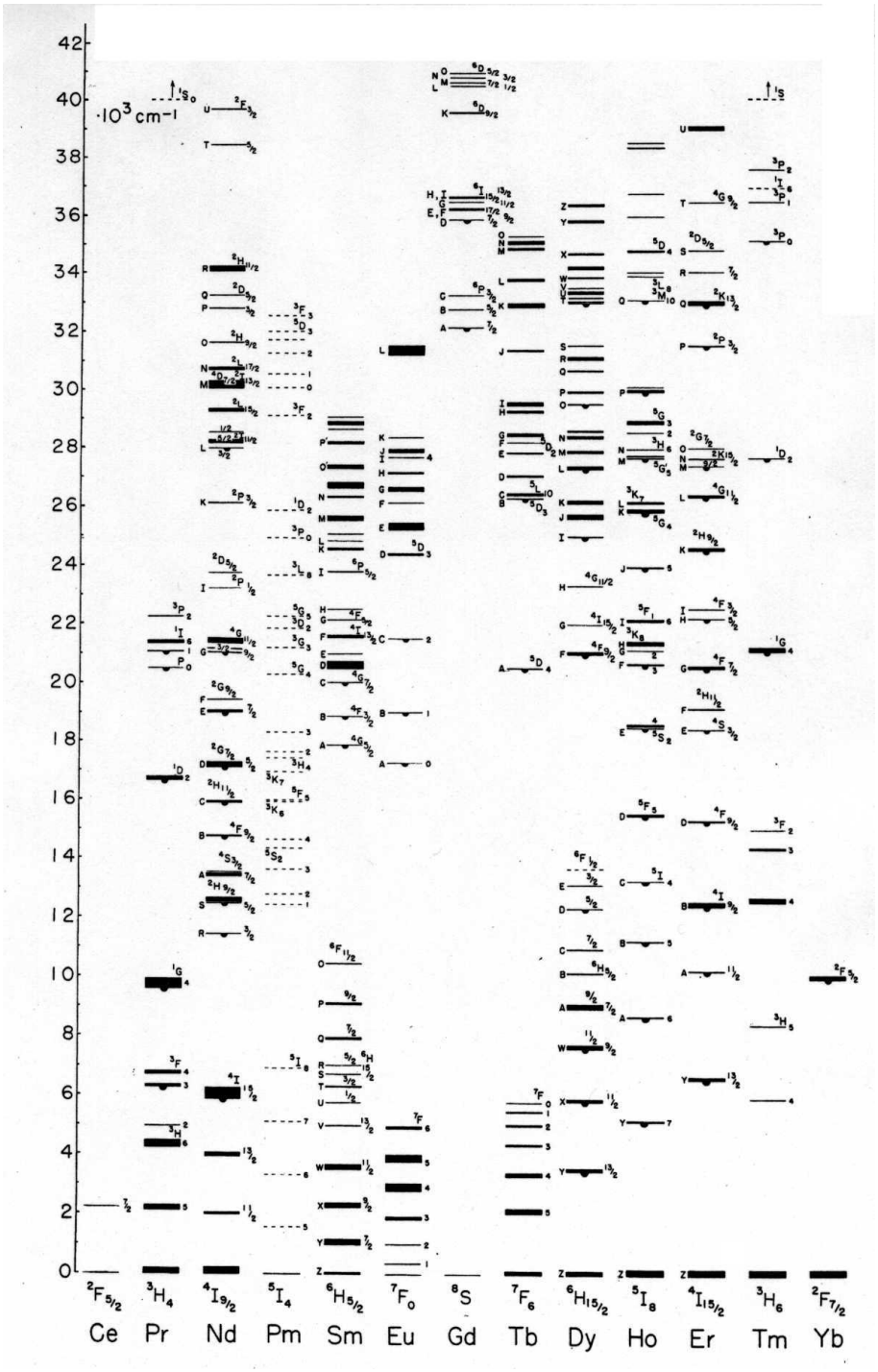

Figure 2.1: Dieke diagram for trivalent lanthanide ions [16]. Energy (in 10^3 cm^{-1}) is shown on the y-axis. $4f$ energy levels of all the lanthanides are drawn, with their respective term symbol. The width of the bars gives the crystal field splitting, which is small compared to transition metal ions.

2.1.3 $f - d$ transitions

For all lanthanide ions, $4f - 5d$ transitions can occur as well [17], in which an electron is excited from the $4f$–shell to the $5d$–shell of the electron cloud. These transitions are parity allowed, which means that absorption is usually strong. A large amount of energy is required to bring the electron into the d–shell, and therefore the absorption bands for these transitions usually lie in the UV region. Because the $d - f$ transitions are parity allowed as well, the lifetime of an excited $4f^{n-1}d^1$ state is typically short, on the order of a few hundred ns. Emission and excitation peaks are typically quite broad. This broad spectral shape is caused by a large offset between the parabolas that are used to describe the $4f$ and $5d$ in a configurational coordinate diagram [15]. The crystal field splitting of $5d$ states is large, because there is a strong interaction between electrons in the $5d$ orbital and the surrounding ligands.

2.2 Förster resonance energy transfer (FRET)

Förster resonance energy transfer (FRET) describes a mechanism where two luminescent centers are involved: a donor and an acceptor. If the donor is excited to a higher energy state by incoming light, it can decay back to the ground state (non-radiatively or radiatively) or transfer its energy to the acceptor. This energy transfer can occur via two main mechanisms: radiative and radiationless transfer. Radiative transfer is a process in which the donor emits a photon and this photon is consecutively absorbed by the acceptor. This radiative transfer always occurs, but non-radiative transfer will dominate at short distances. The non-radiative process is known as FRET and involves a virtual photon which is emitted by the donor and immediately absorbed by the acceptor. The FRET process is only efficient at very short ranges: the rate of FRET decreases with the distance between the donor and acceptor to the power of six. This can be seen in Eq. (2.2) in which γ_{FRET} is the rate of the FRET. The sixth power appears due to the dipole-dipole interaction between donor and acceptor. $C_{don \to acc}$ is a constant which is dependent on the nature of the molecules or ions involved but not on the distance between donor and acceptor. According to Henderson and Imbusch this constant is dependent on the spectral overlap between donor and acceptor ions, as well as the transition dipole moments of the transitions involved [6]. From now on we will refer to this constant as the "donor-acceptor strength".

$$\gamma_{\mathrm{FRET}} = \frac{C_{\mathrm{don} \to \mathrm{acc}}}{r^6} \tag{2.2}$$

FRET is mainly known for its use in biochemistry. Here, a donor and acceptor fluorophore are attached to two different proteins. The sample with proteins and attached fluorophores is then illuminated with short-wavelength (e.g. UV) light which directly excites the donor. If the proteins are close to each other, emission from the acceptor can be detected. If this is not the case, only emission from the donor can be observed.

FRET is not limited to biomolecules, however: it can also occur with transition metal or lanthanide ions as donor and acceptor centers. An example is the spectral conversion of ultraviolet (UV) light inside a fluorescent light bulb. Inside the bulb, UV light is produced by an electrical arc through vaporized mercury. This light is then converted to visible light by three different phosphors: one for blue, one for green and one for red light. An example is the phosphor $LaPO_4$: Ce^{3+}, Tb^{3+}, which emits green light. FRET is the mechanism responsible for this transfer: the UV light is absorbed by the Ce^{3+} ion and the energy is subsequently transferred by FRET to the Tb^{3+} ion. The excited Tb^{3+} ion then decays to a lower energy state by emitting a green photon.

An advantage of the FRET mechanism is that two ions with different properties can be used. In the previous example, the Ce^{3+} ion has a high absorption for UV light due to the parity-allowed nature of the $4f \rightarrow 5d$ transition. The Tb^{3+} ion is an efficient emitter of light: even though the green light emitting transition ${}^5D_4 \rightarrow {}^7F_0$ is parity-forbidden, the ion eventually has to decay back to the ground state. Non-radiative decay is unlikely due to the large difference in energy between the two states. Therefore, only radiative decay occurs and the Tb^{3+} ion efficiently emits green light. If only Tb^{3+} was used in the phosphor, the light output would be low due to the weak absorption.

2.2.1 The Förster radius

For FRET, an often used parameter is the so-called Förster radius (R_0). This is the distance between two ions for which the rate of transfer is exactly the same as the radiative decay rate, which describes simple decay from excited to ground state. This means that, upon excitation, the ion is equally likely to undergo direct luminescence decay as transfer to the acceptor ion. A large value of the Förster radius means that the transfer process is more efficient. If the radiative decay rate of the donor and the transfer strength are known, the Förster radius can be calculated by equating the radiative decay rate with the FRET rate over a distance equal to the Förster radius:

$$\gamma = \gamma_{\mathrm{FRET}}|_{r=R_0} = \frac{C_{\mathrm{don}\rightarrow\mathrm{acc}}}{R_0^6} \tag{2.3}$$

After rearranging we obtain:

$$R_0 = \sqrt[6]{\frac{C_{\mathrm{don}\rightarrow\mathrm{acc}}}{\gamma}} \tag{2.4}$$

The same procedure can be used for migration from a donor to another donor ion by means of FRET.

2.3 Luminescence decay curves

When studying luminescence processes, it is often useful to study how the luminescence intensity develops after excitation of luminescent centers. This can be done by exciting these centers with a laser pulse and monitoring the luminescence intensity over time. This causes the centers to enter excited states from which luminescence takes place; a center in the ground state does not exhibit luminescence. In general, the luminescence will decrease over time, because the population of the emissive excited decreases as luminescent centers return to the ground state.

In this work, we neglect non-radiative decay (multi-phonon relaxation) because it only occurs if the energy difference between excited state and ground state is small. As a rule of thumb, non-radiative decay can be important if the energy difference ΔE is less than five times the maximum phonon energy. The maximum phonon energy for phosphates is around 1100 cm^{-1} [18], whereas the Ce^{3+} $5d^1 \rightarrow 4f^1$ transition in $LaPO_4$ is around 36500 cm^{-1} and the Gd^{3+} ${}^6P_{7/2} \rightarrow {}^8S$ transition is around 32000 cm^{-1}.

Because the luminescence intensity is caused by an ensemble of ions in the excited state that emit photons, the luminescence intensity will always be proportional to the total number of centers in the excited state:

$$I(t) \propto n(t) \tag{2.5}$$

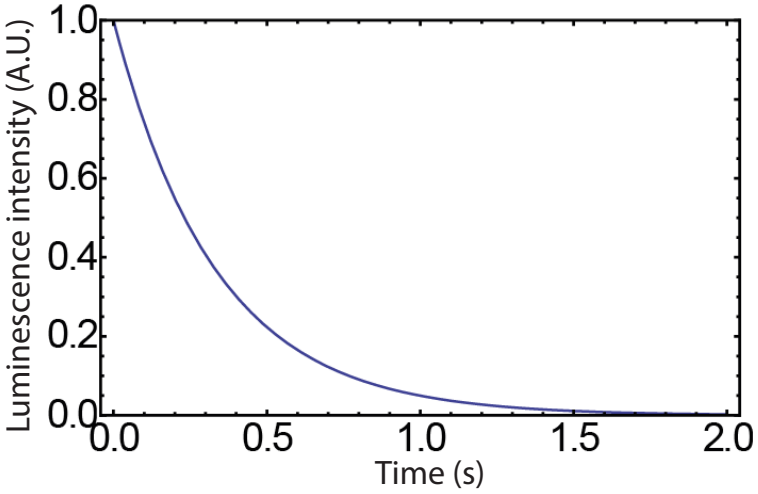

Figure 2.2: Mono-exponential decay, with radiative decay rate $\gamma = 3\ \mathrm{s}^{-1}$ and $n(0) = 1$

How the number of luminescent centers develops over time depends on the nature of the centers and on the chemical and physical environment. We will discuss three different scenarios below: an ensemble of centers without other influences present, a low concentration of centers with acceptor centers, and a high concentration of centers with acceptor centers.

2.3.1 Mono-exponential decay

We have a crystal in which we excite a certain number of donor ions. If a certain number n of luminescent centers of the same type are excited, and only a radiative decay pathway is available, we know that the luminescence is proportional to the number of centers in the excited state. We also know that this luminescence is caused by a radiative decay process which subtracts from the total number of excited states. Therefore we can write:

$$-\frac{dn}{dt} = \gamma n \tag{2.6}$$

Here, dn/dt is the change in number of excited states over time, n is the number of excited states, and γ is the radiative decay rate. From the differential equation it is possible to obtain an expression for the number of excited states as a function of time. The solution of the differential equation is:

$$n = n(0) * e^{-\gamma t} \tag{2.7}$$

This equation is plotted in Fig. 2.2. The shape of the curve is the same as the shape of a luminescence decay curve that is measured in practice. For clarity reasons, a log plot is usually used. In a log plot, a single mono-exponential decay is a straight line; this makes it more convenient to observe deviations from mono-exponential decay. $n(0)$ is the number of centers that are in the excited state at $t = 0$. The constant γ says something about how fast the population of excited states decays: a higher value for γ means a faster decay. The parameter γ is also known as the

radiative decay rate. The inverse of this parameter is known as the *lifetime* of the decay; it is the average time that one luminescent center takes to decay back to the ground state.

2.3.2 Decay with acceptors

If acceptors are present in the lattice, and we neglect non-radiative decay, there are two different pathways for the donor to decay: radiative decay and energy transfer to the acceptor. Therefore the decay rate Γ is composed of two parts:

$$\Gamma = \gamma + \gamma_{\mathrm{ET}} \tag{2.8}$$

We also know that only the donors that decay radiatively contribute to the luminescence. From this it seems easy to derive a new equation for the decay of the amount of donors in the excited state. However, we have to take into account that not all donors have an equal distribution of acceptors around them and therefore the γ_{ET} is different for all donors. This causes the decay to be non-exponential because the expression for $n(0)$ will be a sum of many different exponential functions. The most convenient way to order these functions is to group cation sites in 'shells'. The crystals neighbor list ($\mathbf{n}$,$\mathbf{r}$) gives for each shell i the number of cation sites n_i on distance r_i from the central donor. The environment of a single donor can then be completely described by an array $\mathbf{m}$ giving for each shell i the number m_i of cation sites actually occupied by an acceptor. For a donor with environment $\mathbf{m}$ each nearby acceptor adds $C_{\mathrm{don}\to\mathrm{acc}}/r^6$ (with r the donor-acceptor distance and $C_{\mathrm{don}\to\mathrm{acc}}$ the 'donor-acceptor strength' which depends on the types of donor and acceptor under consideration) to the FRET rate. The total decay rate of a donor with environment m is then given by

$$\Gamma(\mathbf{m}) = \gamma + C_{\mathrm{don}\to\mathrm{acc}} \sum_{i}^{\mathrm{shells}} \frac{m_i}{r_i^6}. \tag{2.9}$$

The probability to find an environment $\mathbf{m}$ can be calculated when considering two things: (i) the acceptor occupations of shells i and $j \neq i$ are not correlated, and (ii) for each shell i the probability to find m_i is binomially distributed, depending on the number of cation sites n_i and the ensemble averaged fraction ϕ of cation sites occupied by an acceptor (the 'acceptor concentration').

$$\begin{aligned} P(\mathbf{m}) &= \prod_{i}^{\mathrm{shells}} p(m_i); \\ p(m_i) &= \binom{n_i}{m_i} \phi^{m_i} (1-\phi)^{n_i - m_i} \end{aligned} \tag{2.10}$$

Now we can write an expression for $n(t)$ as a sum over the decays of excited donors of different environments, with the appropriate weights.

$$n(t) = n(0) \sum_{\mathbf{m}} P(\mathbf{m}) e^{-\Gamma(\mathbf{m})t}, \tag{2.11}$$

where the summation runs over the possible values of m_i for all shells i. Filling in (2.9) and (2.10) yields after some algebra that

$$n(t) = n(0) e^{-\gamma_{rad} t} \prod_{i}^{\mathrm{shells}} \sum_{m_i=0}^{n_i} p(m_i) e^{-C_{\mathrm{don}\to\mathrm{acc}} m_i t / r_i^6}. \tag{2.12}$$

Using (2.7) and the binomial theorem $(A+B)^n = \sum_{k=0}^{n} \binom{n}{k} A^k B^{n-k}$ we arrive at

$$n(t) = n(0)e^{-\gamma_{rad}t} \prod_{i}^{\text{shells}} \left(1 - \phi + \phi e^{-C_{\text{don}\to\text{acc}}t/r_i^6}\right)^{n_i} \tag{2.13}$$

Each factor i in the product accounts for the effect of FRET to shell i on the decay curve. Factor i is approximately equal to unity if $C_{\text{don}\to\text{acc}}t/r_i^6 < 1$, i.e. shells far away hardly affect the decay curve (at least for times sufficiently short after the excitation pulse). This is a direct effect of the short range of FRET. For the upper limit of the product in (2.10) one can choose some value N for which $r^6 N > C_{\text{don}\to\text{acc}}t^*$, where t^* is e.g. the time after which the PL decay curve has reached the background intensity or decayed over 3 orders of magnitude.

2.3.3 Decay with a high concentration of donors and acceptors

If there is a high concentration of donors and acceptors, the problem of finding an expression for $n(t)$ like in the previous section is generally too complex to be solved analytically. However, for two limiting cases an exact solution can still be found: if the donor-donor migration very fast compared to the donor-acceptor transfer rate, and if the donor-donor migration is very slow compared to the donor-acceptor transfer rate.

If the donor-donor migration is vanishingly slow, it can be neglected and the expression for $n(t)$ becomes the same as (2.13). The high concentration of donors does not play a role here, because there is no migration involved and neighboring donor ions act as inert ions.

If the donor-donor migration is very fast compared to donor-acceptor transfer, the excitation travels over so many donor ions that it senses an average environment of acceptor ions. To calculate the average transfer rate, we have to perform the following summation [6]:

$$\langle \gamma_{\text{ET}} \rangle = \phi \sum_{i=1}^{\text{shells}} \frac{C_{\text{don}\to\text{acc}} n_i}{r_i^6} \tag{2.14}$$

where the sum runs over the rate to all lattice sites ($\frac{C_{\text{don}\to\text{acc}} n_i}{r_i^6}$), multiplied by ϕ, the acceptor concentration. Physically, the situation is that all donors have an equal probability of being excited. The decay is now bi-exponential, with decay rate:

$$\gamma + \phi \sum_{i=1}^{\text{shells}} \frac{C_{\text{don}\to\text{acc}} n_i}{r_i^6} \tag{2.15}$$

In the intermediate region, in which the donor-donor migration strength is comparable to the donor-acceptor strength, it is difficult to obtain a direct expression for $n(t)$. In the 60s and 70s, several attempts were made to approximate decay curves at high dopant concentrations by comparing energy migration to other physical processes. In 1967, Yokota and Tanimoto treated the migration of excitation among donors as a diffusion process [8]. However, this has a major drawback: in a diffusion process, diffusion over very small distances is allowed. In reality, luminescent centers are located at fixed positions in a crystal structure and only migration to ions at specific distances can occur. A second approach is to treat the migration of excitation over donor ions as a random walk process [19]. However, all distances between donor and acceptor ions were allowed here as well.

The use of a computer model, in which the donor-to-donor strength is optimized to yield the best possible correspondence with the data, appears therefore very appropriate. In a computer model, a crystal structure can be built in which the luminescent ions assume a fixed position. This approach requires high computation powers, which were not available in the previous century.

2.4 Monte Carlo simulations

Rapid advances in computing technology allow us to study the process of energy migration and transfer using Monte Carlo simulations. The Monte Carlo method refers to a method that relies on repeated random sampling to obtain numerical results. It is often used when it is not feasible to obtain a closed-form expression.

It has proven difficult to obtain a closed-form expression for $n(t)$ at high dopant concentrations, and a donor-donor migration strength which is comparable to the donor-acceptor transfer strength. Therefore it is logical to use the Monte Carlo method to try to obtain an expression for $n(t)$ in this situation. The approach here is to simulate a crystal with random distributions of dopant ions. If the exact distribution is known, we know the distance between every donor-donor and donor-acceptor pair. The problem can then be solved analytically to yield an expression for $n(t)$. This is however still a microscopic expression which describes a very small crystal. Repeating this simulation a large number of times and averaging yields an expression for the macroscopic behavior of $n(t)$. The method used to derive this expression for $n(t)$ was for the most part developed by Freddy Rabouw and described in the next section.

2.4.1 Formulas

We simulate a crystal with donor and acceptor ions. An excitation laser pulse instantaneously excites a subset of the donor ions. The approach here is to derive for each ion a differential equation that describes its behavior over time. The population of donor i evolves as

$$\begin{aligned}\frac{dn_i}{dt} &= -\gamma n_i + \sum_{j\neq i}^{\text{don}} M_{i\leftrightarrow j}[(1-n_i)n_j - n_i(1-n_j)] - \sum_{k}^{\text{acc}} T_{i\leftrightarrow k} n_i \\ &= -\gamma n_i + \sum_{j\neq i}^{\text{don}} M_{i\leftrightarrow j}[n_j - n_i] - \sum_{k}^{\text{acc}} T_{i\leftrightarrow k} n_i\end{aligned} \tag{2.16}$$

with n_i the probability that donor ion i is in the excited state, γ the radiative decay rate of the donor ions, $M_{i\leftrightarrow j}$ the donor-to-donor energy migration rate, and $T_{i\leftrightarrow k}$ the donor-to-acceptor energy transfer rate. Note that $M_{i\leftrightarrow j}$ and $T_{i\leftrightarrow k}$ strongly depend on the distance between the ions involved. The first term of the equation describes pure radiative decay; it is negative because radiative decay always causes a decrease in the ion population. The second term in the equation describes both energy migration from i to j and the reverse process of energy migration from j to i, for which we assume equal rates. It can be both positive or negative because a migration from ion i to j subtracts from the population of ion i whereas a migration from ion j to i adds to the population of ion i. The third term describes transfer to an acceptor center; it is always negative because transfer from a donor to an acceptor always subtracts from the ion population. Back-transfer from an acceptor to a donor is not taken into account because it can usually be neglected.

The above equation is a linear set of (differential) equations, which can be rewritten in the matrix form. Basically this means that we rewrite the equation as $\frac{d}{dt}\mathbf{n} = \mathbf{A}\mathbf{n}$, in which $\mathbf{n}$ is a

vector denoting every ion n_i and $\mathbf{A}$ is a matrix. After rewriting we obtain

$$\mathbf{A} = \begin{pmatrix} -\Gamma_1 & M_{1\leftrightarrow 2} & M_{1\leftrightarrow 3} & \cdots & M_{i\leftrightarrow j} \\ M_{2\leftrightarrow 1} & -\Gamma_2 & M_{2\leftrightarrow 3} & & \\ M_{3\leftrightarrow 1} & M_{3\leftrightarrow 2} & -\Gamma_3 & & \\ \vdots & & & \ddots & \\ M_{j\leftrightarrow i} & & & & -\Gamma_i \end{pmatrix} \tag{2.17}$$

If we multiply this matrix with the vector $\mathbf{n}$ we obtain equation (2.8). The general solution of this system of rate equations is

$$\mathbf{n}(t) = \sum_i c_i \mathbf{v}_i \mathrm{e}^{-\gamma_i t} \tag{2.18}$$

where γ_i and $\mathbf{v}_i$ are the eigenvalues and corresponding eigenvectors of rate matrix $\mathbf{A}$. The coefficients $\{c_i\}$ are determined by the initial distribution of excitation energy $\mathbf{n}(0)$:

$$\mathbf{c} = \mathbf{V}^{-1}\mathbf{n}(0) \tag{2.19}$$

with $\mathbf{V} = (\mathbf{v}_1\ \mathbf{v}_2\ \mathbf{v}_3\ ...)$. Hence, following the excitation of a single donor k the population evolution is described by Eq. 5 with $c_i = c_i^{(k)} = (V^{-1})_{ki}$.

For a particular excitation distribution $\mathbf{n}(0)$, the light intensity recorded after time t is proportional to the total population of excited donors:

$$I(t) \propto \sum_j^{\mathrm{don}} n_i(t) = \sum_i \left(c_i \sum_j^{\mathrm{don}} V_{ij} \mathrm{e}^{-\gamma_i t} \right) \tag{2.20}$$

If we assume that the excitation power is low and saturation of the acceptor centers is not a factor, the experimental photoluminescence decay curve results from averaging (2.12) over all possible single-donor excitations k:

$$\begin{aligned} I(t) \propto \sum_k^{\mathrm{don}} \sum_j^{\mathrm{don}} n_j^{(k)}(t) &= \sum_i \left(\sum_k^{\mathrm{don}} c_i^{(k)} \sum_j^{\mathrm{don}} V_{ij} \mathrm{e}^{-\gamma_i t} \right) \\ &= \sum_i \left(\sum_k^{\mathrm{don}} (V^{-1})_{ki} \right) \left(\sum_j^{\mathrm{don}} V_{ij} \right) \mathrm{e}^{-\gamma_i t} \end{aligned} \tag{2.21}$$

where $n_j^{(k)}(t)$ denotes the probability that donor ion j is excited after time t following initial excitation in donor ion k. We see that the decay curve contains rate components $\{\gamma_i\}$ with weights $\{\left(\sum_k^{\mathrm{don}} (V^{-1})_{ki} \right) \left(\sum_j^{\mathrm{don}} V_{ij} \right)\}$.

2.4.2 Periodic boundary conditions

If we model a crystal of finite size, ions at the surface will have fewer neighbors than others. Because in reality we will deal with large, annealed crystals in which the surface area is low compared to the volume, this is not a physically relevant situation. Therefore we will impose periodic boundary conditions, which means that the same crystal is repeated several times in space. To simulate this situation, we impose the condition that the box size length is subtracted from the distance between two ions if their distance is larger than half the box size length. This procedure is followed for all three unit cell dimensions.

2.4.3 Modeled decay curves

To create modeled decay curves we first have to build a crystal lattice. This can be done by considering the crystal structure: monocline (monazite, $LaPO_4$) and tetragonal bipyramidal (xenotime, YPO_4). The unit cell distances and angles were obtained from literature [20]. Both monazite and xenotime have four cation positions per unit cell. The distance between two cations can be calculated by adding the distance between the unit cells to the distance between the positions of the ions within the unit cell, taking into account the periodic boundary conditions. If we know the distance between the ions, we can calculate all values of matrix (2.17). The migrations rates M and the transfer rates T are calculated using the following equations:

$$M_{i \leftrightarrow j} = C_{\text{don-don}} r_{ij}^{-6} \tag{2.22}$$

$$T_{i \leftrightarrow k} = C_{\text{don-acc}} r_{ik}^{-6} \tag{2.23}$$

The constant $C_{\text{don-acc}}$ can be approximated by doing experiments on samples with low donor concentration (see section 2.3.2). The constant $C_{\text{don-don}}$ is an unknown fit parameter. It is one of the main aims of this research to obtain the value of $C_{\text{don-don}}$ for both model systems and compare it to the value of $C_{\text{don-acc}}$.

2.4.4 Number of simulations and box size

Two important parameters in the model are the box size and the number of simulations. If the box size is too small, a small box of similarly located donor and acceptor ions is repeated infinitely in each direction due to the periodic boundary conditions. This situation is unphysical, because donor and acceptor ions are distributed randomly in a real crystal. However, if the box size is large enough, the distribution will approximate a completely random distribution.

The number of simulations is an important parameter as well. In practice, we study luminescence of a sample that contains on the order of N_{av} $(6.02 * 10^{23})$ atoms. If we were to simulate a box size which contains this many atoms, it would take a huge amount of computing time and power. However, we can also keep the box size smaller and repeat the simulation multiple times. This is physically the same as exciting different parts of a large crystal with a laser pulse. By carefully tuning the box size as well as number of simulations, we can model a physically relevant situation while limiting computing time and power.

In this work, we will always work with a box size of 7x7x7 and a number of simulations of 1.000 unless otherwise noted. In the monazite and xenotime unit cell, each unit cell contains four different Ln^{3+} cations. This means that the box contains $7 * 7 * 7 * 4 = 1372$ cations.

We can verify that the box size and number of simulations is sufficient by gradually increasing the box size and number of simulations. At a certain point, the simulated decay curves will not change significantly anymore and we have reached the point of convergence. If this point has been reached before we reach a box size of 7x7x7 and a number of simulations of 1.000, we have verified that the chosen parameters are sufficient. The influence of the box size can be seen in Fig. 2.3, the influence of the number of simulations can be seen in Fig. 2.4. We see that indeed, the point of convergence is reached after 1000 simulations and a box size of 7x7x7.

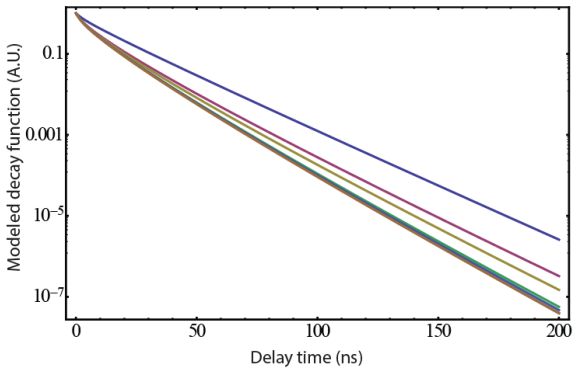

Figure 2.3: Modeling the $LaPO_4$: Ce^{3+}, Nd^{3+} system with different box sizes: a box size of 2 (blue), 3 (red), 4 (yellow), 5 (green), 6 (light blue), 7 (magenta) and 8 (orange). The functions of 7 and 8 overlap almost completely. Other parameters are: number of simulations (1000), Ce^{3+} lifetime (16.66 ns), Ce^{3+}–Nd^{3+} transfer rate (0.0025 $ns^{-1}Å^6$), Ce^{3+}–Nd^{3+} migration rate (0.0025 $ns^{-1}Å^6$), Ce^{3+} concentration (5%) and Nd^{3+} concentration (5%)

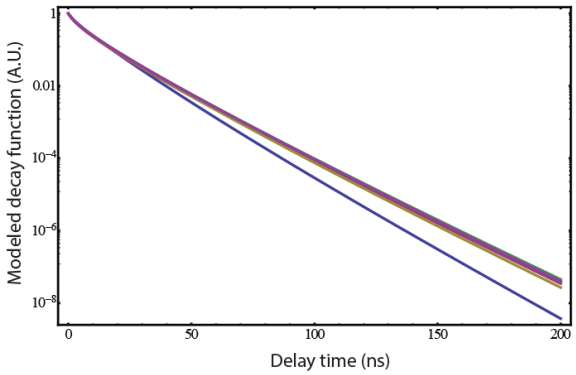

Figure 2.4: Modeling the $LaPO_4$: Ce^{3+}, Nd^{3+} system with different number of simulations: 1 simulation (blue), 5 (red), 25 (yellow), 125 (green), 625 (light blue) and 3125 simulations (magenta). The functions of 625 and 3125 overlap almost completely. Other parameters are: box size (7), Ce^{3+} lifetime (16.66 ns), Ce^{3+}–Nd^{3+} transfer rate (0.0025 $ns^{-1}Å^6$), Ce^{3+}–Nd^{3+} migration rate (0.0025 $ns^{-1}Å^6$), Ce^{3+} concentration (5%) and Nd^{3+} concentration (5%)

2.4.5 Influence of the crystal structure

In this work we study energy migration in two different crystal structures: monazite ($LaPO_4$) and xenotime (YPO_4). The distances between ions in these two lattices is different and the transfer and migration rates between ions will also differ. Consequently, the decay curves will have a different shape for the two crystal structures. The analytical expression (neglecting donor-donor migration) will differ because the two crystal structures have a different neighbor list (see section 2.3.2). The decay curves created with Monte Carlo methods will differ as well because a different rate matrix is created (see section 2.3.3).

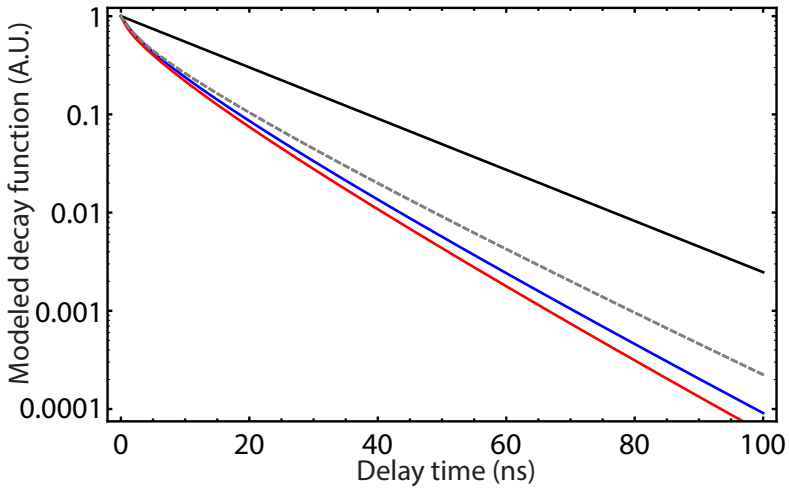

Figure 2.5: Modeling the Ce^{3+} and Nd^{3+} system within the monazite structure (blue) and the xenotime structure (red). Pure radiative decay is indicated by the black line. The dashed gray line represents an analytical expression neglecting donor-donor migration: there is no observable difference between the analytical expressions for monazite and xenotime. Parameters are: Ce^{3+} lifetime (16.66 ns), Ce^{3+}–Nd^{3+} transfer rate (0.0025 $ns^{-1}Å^6$), Ce^{3+}–Ce^{3+} migration rate (0.0025 $ns^{-1}Å^6$), Ce^{3+} concentration (5%) and Nd^{3+} concentration (5%).

It is known that $LaPO_4$ crystallizes in the monazite structure whereas YPO_4 crystallizes in the xenotime structure. However, trying to model the luminescent decay with different crystal structures can provide useful insights into the energy transfer dynamics.

In Fig. 2.5, the difference between the two crystal structures is shown for the ion pair Ce^{3+} and Nd^{3+}. Only the blue line has physical relevance, because we know that $LaPO_4$: Ce^{3+}, Nd^{3+} crystallizes in the monazite structure. It can be seen that the difference between the model at different crystal structures is small. The predicted slightly faster decay for the xenotime can be explained by the closer nearest-neighbor distance (0.38 nm vs 0.41 nm). It is interesting to note that there is no observable difference if an analytical expression is used which neglects migration; the difference in expressions is probably too small to be observed.

In figure 2.6, the same difference between the two crystal structures is shown for the ion pair Gd^{3+} and Er^{3+}. Only the red line has physical relevance, because we know that YPO_4: Gd^{3+}, Er^{3+} crystallizes in the monazite structure. Similarly as for the Ce^{3+} and Nd^{3+} pair, the difference between the crystal structures is small, but the decay is predicted to be faster if a xenotime structure is used. The analytical expression also predicts a faster decay for the xenotime structure.

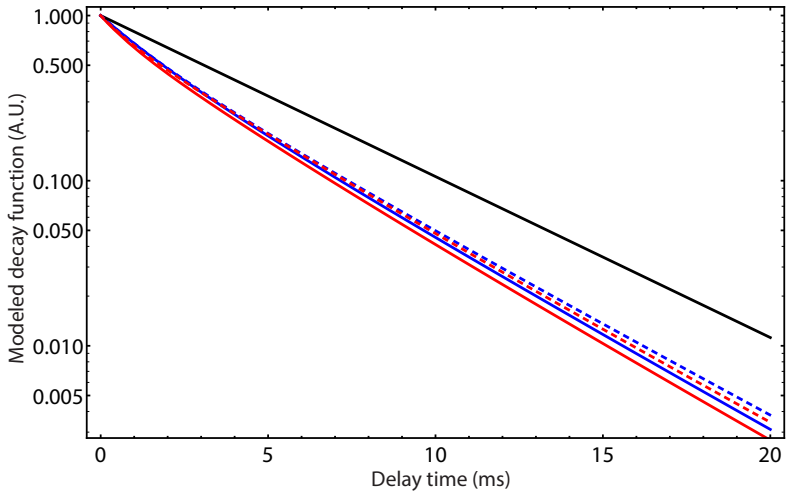

Figure 2.6: Modeling the Gd^{3+} and Er^{3+} system within the monazite structure (blue) and the xenotime structure (red). Pure radiative decay is indicated by the black line. The dashed lines represent analytical expressions neglecting donor-donor migration: monazite (blue) and xenotime (red). Parameters are: Gd^{3+} lifetime (4.454 ms), Gd^{3+}–Er^{3+} transfer rate (0.0026 $ms^{-1}Å^6$), Gd^{3+}–Gd^{3+} migration rate (0.0026 $ms^{-1}Å^6$), Gd^{3+} concentration (5%) and Er^{3+} concentration (5%).

2.4.6 Adding a background signal

In order to properly compare the luminescence decay measurements with the modeled decay curves, it is convenient to add a background to the modeled decay curves. We know from experience that the intensity of this background is around 10^{-4} of the peak signal. If we add this background to the modeled decay function, a more reasonable comparison with the experimental data can be made.

Chapter 3

Experimental Section

3.1 Synthesis

Synthesis of the $LaPO_4$: Ce^{3+}, Nd^{3+} model system was based on a synthesis developed by van Schaik et al. [21]. This procedure was optimized for high crystallinity as judged from X-ray diffraction (see measurements section). Appropriate amounts of rare earth oxides were mixed with a stoichiometric amount of $(NH_4)_2HPO_4$ and crushed in a ball mill for 10 minutes, using acetone as lubricant. After evaporation of the acetone, the samples were heated in a tubular oven to 1100°C for 3 hours. The samples were then crushed in a ball mortar for 10 minutes and heated to 1400°C for 3 hours in a tubular oven under H_2 pressure. X-ray diffraction was used to confirm that the samples were phase pure (see section 4.1).

The coprecipitation synthesis of the YPO_4: Gd^{3+}, Er^{3+} model system was based on a synthesis developed by Vergeer et al. [2] and a rare earth chloride synthesis by Meyer et al. [22]. Appropriate amounts of rare earth oxides were mixed with a 15x excess of NH_4Cl. Heating to 240°C for 10 hours converted the oxides to chlorides. The chlorides were subsequently dissolved in H_2O and a 110% excess of oxalic acid (aqueous solution) was added. Precipitation of rare earth oxalates occurred instantaneously. The suspension was washed three times by centrifugation, removal of the supernatant and addition of fresh water in order to remove excess chloride ions. The resulting rare earth oxalates were dried and subsequently converted to oxides by heating to 1100°C for 3 hours. Finally, the oxides were mixed with a stoichiometric amount of $(NH_4)_2HPO_4$ and heated to 1400°C for 3 hours. An X-ray diffractogram of the samples was measured and the samples appeared to be phase pure (see section 4.1). The YPO_4: Gd^{3+}, Er^{3+} model system was also synthesized with the solid state method; this was performed in the exact same way as for the $LaPO_4$: Ce^{3+}, Nd^{3+} model system.

3.2 Characterization

X-ray diffraction (XRD) patterns were recorded with a Philips PW1729 X-ray diffractometer using CuKα radiation ($\lambda = 1.5418$ nm).

Emission and excitation spectra were measured using an Edinburgh Instruments FLS920 fluorescence spectrometer equipped with a 450 W xenon lamp and double excitation monochromator with a grating blazed at 300 nm for excitation of Ce^{3+} ions. For lifetime measurements on $LaPO_4$:

Ce^{3+} and $LaPO_4$: Ce^{3+}, Nd^{3+}, excitation was carried out with a PicoQuant pulsed diode laser (PDL 800-B and PLS 8-2-409) emitting at 270 nm (repetition rate 2.5 MHz). For UV/Vis detection of the decay curves, a Hamamatsu H742202 photomultiplier tube was used. Analysis was carried out using time-correlated single photon counting (TCSPC). For lifetime measurements on YPO_4: Gd^{3+} and YPO_4: Gd^{3+}, Er^{3+} excitation was carried out using an Opolette HR 355 optometric parametric oscillator (OPO). Detection was carried out using an Ekspla K928 photomultiplier tube and analysis was carried out using a multi-channel scaling (MCS) method.

Chapter 4

Results and Discussion

4.1 X-ray diffraction

The powders which were synthesized are mostly ordered (crystalline) but disordered (amorphous) regions within the powders can exist as well. The relative amount of crystalline material within the powder is referred to as the "crystallinity". To measure the crystallinity of the synthesized powders, X-ray diffraction was used. X-ray diffraction can determine the crystallinity of the synthesized powders. Higher peaks in an X-ray diffractogram correspond with a higher degree of crystallinity, because the reflection on the Bragg planes is stronger. It can also determine whether the powders are single-phase (one crystal structure) or multi-phase (mixed crystal structures).

Rare earth phosphates adopt two main crystal structures: monazite (monocline) and xenotime (tetragonal bipyramidal). The fact that there are two different structures is caused by a difference in ionic radius of the lanthanide ions. The lighter, larger lanthanides (La-Gd) usually adopt the monazite structure whereas the heavier, smaller lanthanides (Gd-Lu) and yttrium (Y) usually adopt the xenotime structure.

Three diffractograms of $LaPO_4$: 5% Ce^{3+}, 5% Nd^{3+}, $LaPO_4$: 16.5% Ce^{3+}, 5% Nd^{3+} and $LaPO_4$: 0.1% Ce^{3+}, 16.5% $Nd^{3+}$are shown on the next page. The experimental measurements are in red, references of the $LaPO_4$ (PDF 01-083-0651) and YPO_4 (PDF 11-254) crystal structures are indicated by black bars. The samples were also used for luminescence decay curve analysis (see section 4.3). An optimization procedure was carried out for $LaPO_4$ to increase the crystallinity of the powders as much as possible.

As can be seen, there is a good correspondence between the data and the references. Only a few peaks appear that cannot be explained by the monazite and xenotime structure: at $2\theta = 44$ and 63. These peaks are caused by diffractions on the aluminium sample holder. No evidence of second phases, such as Ce (IV) compounds, can be observed in the diffractograms. The high crystallinity and single-phase crystal structure is retained at high Ce^{3+} and high Nd^{3+} concentrations, as can be seen in Fig. 4.2 and 4.3. Therefore it can be assumed that all synthesized $LaPO_4$: Ce^{3+}, Nd^{3+} powders adopt a single-phase monazite structure.

The synthesized YPO_4: Gd^{3+}, Er^{3+} powders were measured with XRD as well. The results are shown in Fig. 4.4 and 4.5. The XRD pattern show that all peaks of the xenotime structure can be detected. However, the sample with high gadolinium content shows a significant decrease in crystallinity (3000 vs. 5500 peak counts). It is possible that a higher Gd^{3+} concentration causes distortions in the crystal structure, lowering the crystallinity.

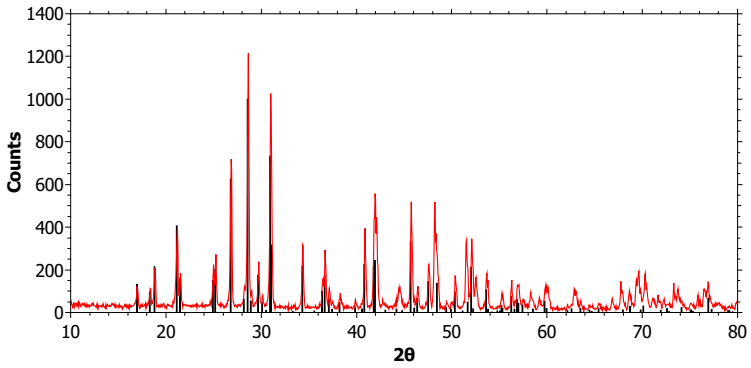

Figure 4.1: XRD pattern of $LaPO_4$: 5% Ce^{3+}, 5% Nd^{3+} (red) with reference (black)

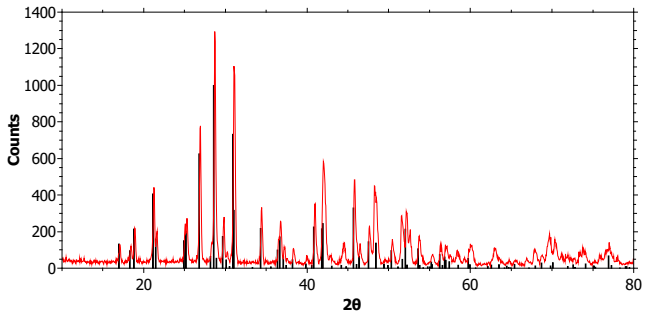

Figure 4.2: XRD pattern of $LaPO_4$: 16.5% Ce^{3+}, 5% Nd^{3+} (red) with reference (black)

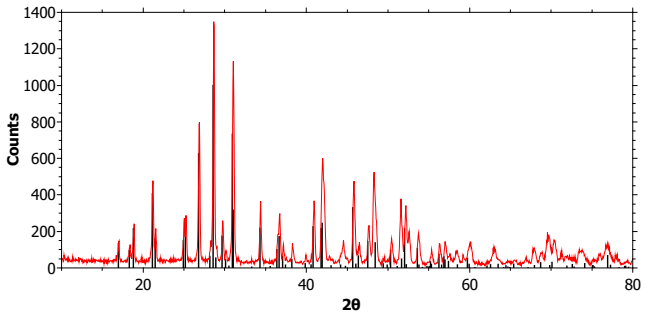

Figure 4.3: XRD pattern of $LaPO_4$: 0.1% Ce^{3+}, 16.5% Nd^{3+} (red) with reference (black)

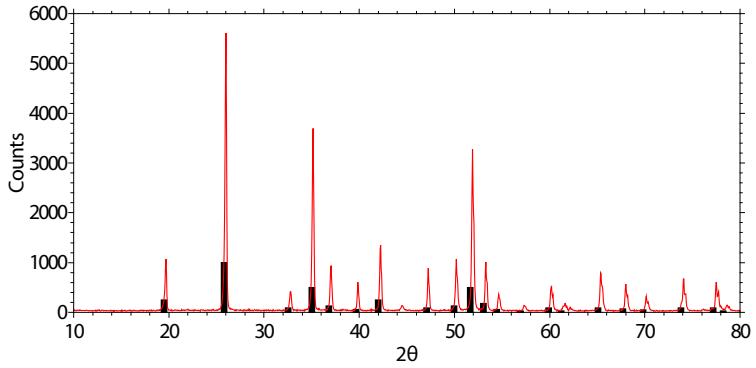

Figure 4.4: XRD pattern of YPO_4: 0.1% Gd^{3+}, 10% Er^{3+} (red) with reference (black)

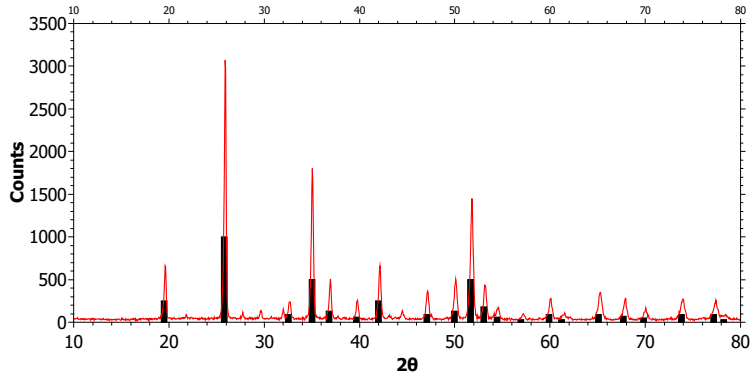

Figure 4.5: XRD pattern of YPO_4: 10% Gd^{3+}, 5% Er^{3+} (red) with reference (black)

4.2 Emission and excitation spectra

A useful tool to investigate the luminescence dynamics inside a phosphor is the recording of emission and excitation spectra. To obtain an emission spectrum, the sample is irradiated with light of a fixed wavelength. The amount of photons emitted from the sample is then recorded at different wavelengths. To obtain an excitation spectrum, the reverse is done: the amount of photons emitted is recorded at a fixed emission wavelength while the excitation wavelength is varied.

4.2.1 Emission and excitation of Ce^{3+}

An emission and excitation spectrum of $LaPO_4$: 1% Ce^{3+} is shown in Fig. 4.6. Both the excitation and the emission spectrum show several broad bands. The spectra can be explained by considering the different energy levels of the Ce^{3+} ion: the bands in the excitation spectrum can be assigned to $4f^0 5d^1 \rightarrow 4f^1$ transitions while the bands in the emission spectrum can be assigned to $4f^1 \rightarrow 4f^0 5d^1$ transitions. The ground state of the Ce^{3+} ion is $4f^1$. Because the electron is in the $4f$ shell

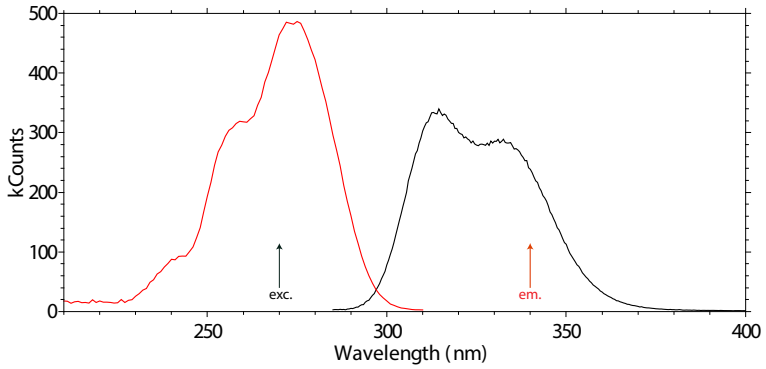

Figure 4.6: Excitation spectrum (red) and emission spectrum (black) of $LaPO_4$: 1% Ce^{3+}. Excitation wavelength (270 nm) is marked with a black arrow, emission wavelength (340 nm) is marked with a red arrow.

and is shielded from the chemical environment, there is to a good approximation no crystal field splitting of this ground state. The ^2F ground state can assume two different J values: $J = 5/2$ and $J = 7/2$, with the former having the lowest energy. The transitions that are related to the bands shown in the spectrum involve excitation of the ion to the $5d$ excited state, which has a term symbol of ^2D. In contrast to the $4f$ shell, this state is strongly affected by the chemical environment and is split by the crystal field. The monazite structure has a symmetry of C_{2h}. According to the character table of this point group, this splits the ^2D excited state into five different states: three ^2A_g and two ^2B_g states. A global energy level diagram of all the different energy levels can be seen in Figure 4.5. Excitation (red) and emission (green) lines are also shown. Excitation of the Ce^{3+} ion can only occur from the ground state. If excitation to the $5d$ orbital occurs, the system rapidly relaxes to the lowest $5d$ level via non-radiative decay. Therefore only emission from the lowest level of the $5d$ state occurs. For these reasons, we expect five different peaks in the excitation spectrum and two different peaks in the emission spectrum. This is indeed what is observed. Two bands can be seen in the emission spectrum with $\lambda = 315$ and 335 nm. In the excitation spectrum, three different bands can be observed at wavelengths of 240, 255 and 275 nm. According to literature [23], the wavelengths should be 206, 214, 239, 256 and 274 nm. This is consistent with our three last observed wavelengths; the first two excitations are probably too weak to be observed. The peaks in both the emission and the excitation spectrum are quite broad, because there is a large interaction between the $5d$ state and the chemical environment.

It is interesting to note that there is a small overlap between the excitation and emission spectrum. In order to achieve energy transfer from a donor to an acceptor, overlap between the emission spectrum of the donor and the excitation spectrum of the acceptor is mandatory. In this work we would like to study energy transfer from one Ce^{3+} ion to another. The overlap between the excitation and emission spectrum shows that this transfer is possible, although the relatively small overlap will probably limit the rate at which this process occurs.

It is possible to study the decay of the Ce^{3+} excited state by exciting and 270 nm and measuring the luminescence decay at 340 nm. This is described in section 4.3.1.

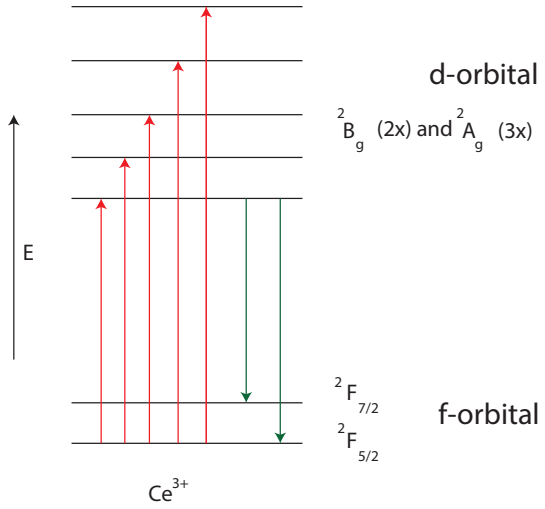

Figure 4.7: Global energy level diagram of the Ce^{3+} ion (energy levels not to scale). Possible excitations are indicated with red, possible emissions with green arrows.

4.2.2 Nd^{3+} emission

In this work we want to quantify the rate at which migration from Ce^{3+} ions to other Ce^{3+} ions occurs. In order to study this process we also have to add acceptor ions. If no acceptor ions are added, migration from Ce^{3+} to Ce^{3+} ions does not significantly alter the luminescence properties of the material; although the eventual quenching on defects or traps may increase, this effect is difficult to quantify. In this work we have chosen the lanthanide Nd^{3+} as an acceptor ion, using the system $LaPO_4$: Ce^{3+}, Nd^{3+}. This is very similar to the system $LaPO_4$: Ce^{3+}, Tb^{3+} which is used in fluorescent light bulbs to convert UV to green light [24]. Although $LaPO_4$: Ce^{3+}, Nd^{3+} is not such a commonly used system, energy transfer from Ce^{3+}, Nd^{3+} has been reported before in the literature [21]. The Nd^{3+} ion has the advantage of being more chemically similar to La^{3+} and Ce^{3+}, making incorporation into the crystal lattice more convenient and reducing the risk of phase separation. This was confirmed by XRD measurements (see section 4.1): the crystallinity of $LaPO_4$: Ce^{3+}, Nd^{3+} was significantly higher than $LaPO_4$: Ce^{3+}, Tb^{3+} and phase separation did not occur.

Some indication of energy transfer from Ce^{3+} to Nd^{3+} can be obtained by exciting Ce^{3+} in the UV region and measuring the emission of Nd^{3+}. Although Nd^{3+} can possibly also be directly excited at 270 nm, the absorption of Ce^{3+} ions is much stronger. Emission spectra of $LaPO_4$: 0.1 % Ce^{3+} with increasing concentration of Nd^{3+} can be seen in Fig. 4.8. Several emissions are visible, however, the emission peaks with $\lambda < 1000$ nm are also present in the sample without Nd^{3+} and are probably not caused by Nd^{3+} emission. Emission from defects or trap is the most likely explanation for these peaks. In contrast, the sharp peak around 1064 nm is not present in the sample without Nd^{3+}, and it can be assigned to the $^4F_{3/2} \rightarrow {}^4I_{11/2}$ transition on the Nd^{3+} ion. A weak emission can also be seen around 1319 nm, which can be assigned to the $^4F_{3/2} \rightarrow {}^4I_{13/2}$ transition. These two emissions offer direct proof of energy transfer from Ce^{3+} to Nd^{3+}. It can be seen that the emission peak heights decrease at higher Nd^{3+} concentration. This is probably

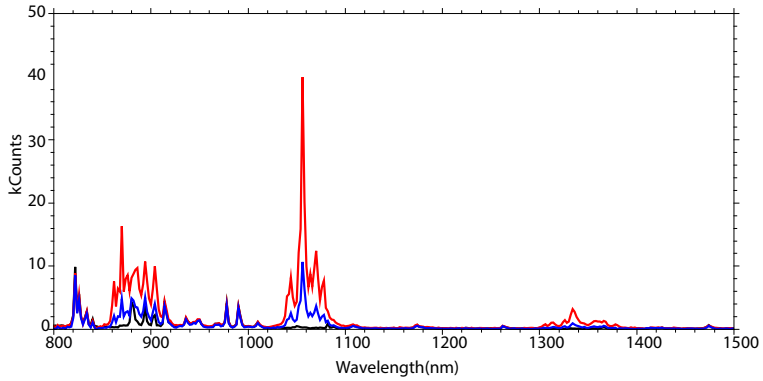

Figure 4.8: Emission spectrum of $LaPO_4$: 0.1% Ce^{3+} with increasing Nd^{3+} concentration: 0% (black), 2.5% (red) and 10 % (blue). Excitation was performed at 270 nm.

caused by quenching of these emissions at higher concentrations, decreasing the luminescence. In conclusion, luminescence from Nd^{3+} ions was detected while exciting in the UV region, and this offers an indication that transfer from Ce^{3+} to Nd^{3+} can occur. More proof about this transfer is apparent from the luminescence decay curves, see section 4.3.1.

4.2.3 Emission and excitation of Gd^{3+}

A similar analysis as in 4.2.2 was carried out for the YPO_4: Gd^{3+}, Er^{3+} system. First, an emission and excitation scan of YPO_4: 0.1 % Gd^{3+} was measured to see where the strongest emission and excitation wavelength is located. The result can be seen in Fig. 4.9.

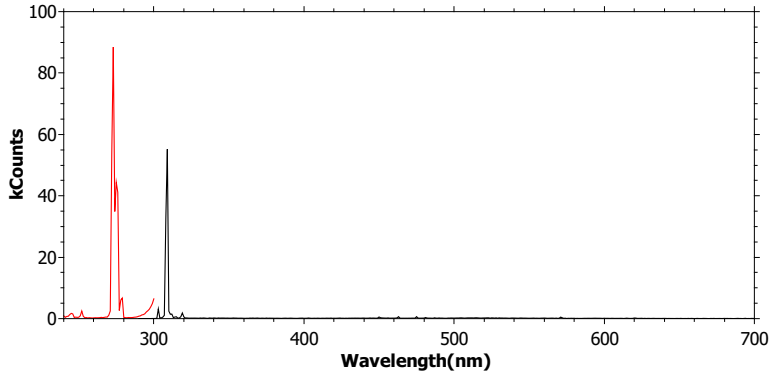

Figure 4.9: Excitation spectrum (red) and emission spectrum (black) of YPO_4: 0.1% Gd^{3+}. Excitation for the emission spectrum was performed at 273 nm, the excitation spectrum was measured while detecting emission at 309 nm. The spectrum was not corrected for detector response.

The spectra are characterized by sharp excitation and emission lines, as can be expected for $f-f$ transitions on a trivalent lanthanide ion. Excitation peaks are located around 273 nm which

can be assigned to various $^8S \rightarrow {}^6I_J$ transitions. The main emission peak is located at 309 nm, which can be assigned to a $^6P_{7/2} \rightarrow {}^8S$ transition. Small side peaks in the emission spectrum are caused by emission from the nearby $^6P_{5/2}$ level, as well as a small crystal field splitting. It is possible to study the decay of the $^6P_{7/2} \rightarrow {}^8S$ by exciting at 273 nm and measuring the emission at 309 nm. This is described in section 4.3.2.

It should be noted that it is not possible to obtain a value for the spectral overlap from Figure 4.9. The relevant spectral overlap for Gd^{3+}–Gd^{3+} migration is the overlap between the $^6P_{7/2} \rightarrow {}^8S$ emission and the $^8S \rightarrow {}^6P_{7/2}$ excitation, which is not visible in the graph and is also difficult to detect experimentally.

4.2.4 Er^{3+} emission

For the second system, Er^{3+} was chosen as an acceptor ion. The reason for this is that this ion fits within the xenotime structure of YPO_4 and that it has many energy levels with a similar energy to the $^6P_{7/2}$ level of Gd^{3+}. An attempt was made to incorporate ions such as Tb^{3+} and Dy^{3+}, but luminescence decay curves for these samples were difficult to fit to an analytical function.

If energy transfer from Gd^{3+} to Er^{3+} occurs, it would be expected that emission from Er^{3+} ions can be detected, similarly to emission from Nd^{3+} ions in section 4.2.2. Typical for Er^{3+} luminescence is the green emission that arises from $^4S_{3/2} \rightarrow {}^4I_{15/2}$ and $^2H_{11/2} \rightarrow {}^4I_{15/2}$ transitions [25].

Contrary to expectations, it was not possible to detect any emission from Er^{3+}, neither for samples synthesized with the coprecipitation method nor for those prepared using the solid state method. Neither was the Er^{3+} emission detected while attempting to directly excite the Er^{3+} ion at lower energies. However, luminescence decay curves of YPO_4: Gd^{3+}, Er^{3+} clearly indicate that energy transfer from Gd^{3+} to Er^{3+} is taking place, and the incorporation of Er^{3+} in the samples was evident from the pink color of samples containing Er^{3+}. Therefore we hypothesize that the Er^{3+} emission is not visible due to rapid cross-relaxation.

Cross-relaxation is a process that is the inverse of an upconversion process: the excited state of an ion (ion 1) falls back to an intermediate state while this energy is concomitantly transferred to another nearby ion (ion 2) [26]. For the cross-relaxation process it is necessary that energy is conserved, i.e. that the energy difference between excited state and intermediate state of ion 1 is similar to the energy difference between the ground state and excited state of ion 2.

We can consider this process for an Er^{3+} ion. If this ion is excited by a Gd^{3+} ion via energy transfer, the ion is most likely excited to the $^2P_{3/2}$ level because this is most close in energy to the $^6P_{7/2}$ excited state of the Gd^{3+} ion (see Dieke diagram, Fig. 2.1).

In Fig. 4.10 a possible cross-relaxation pathway can be seen. The $^2P_{3/2}$ level has an energy difference of around $31.5*10^3$ cm^{-1} with the ground state, while the $^4F_{9/2}$ has an energy difference of around $15.5*10^3$ cm^{-1} with the ground state; cross-relaxation appears to be possible considering the energy conservation criterion.

Because the green emitting $^4S_{3/2}$ and $^2H_{11/2}$ levels can no longer be reached after cross-relaxation, the process could explain why green emission is not present. However, one would still expect red emission from the $^4F_{9/2}$ excited state which was not detected either. In addition, it cannot explain why the emission was not detected when attempting to directly excite the Er^{3+} ions. Possibly, the existence of traps or defects in the lattice is an additional issue which causes the excitation energy to be lost non-radiatively.

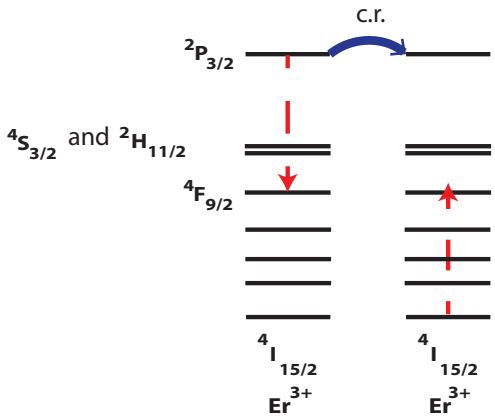

Figure 4.10: Energy diagram with a possible cross-relaxation (c.r.) process of Er^{3+} ions, one of which is excited to the $^2P_{3/2}$ level via energy transfer from excited Gd^{3+} ions. The cross-relaxation process is the relaxation of the $^2P_{3/2}$ level to the $^4F_{9/2}$ state on ion 1 (left) and concomitant excitation from the ground state to the $^4F_{9/2}$ state on ion 2 (right).

4.3 Luminescence decay curves

Luminescence decay curves were recorded using the time-correlated single photon counting (TC-SPC) method for Ce^{3+} emission and multi-channel scaling (MCS) for Gd^{3+} emission. The equipment used is described in the experimental section (3.2).

4.3.1 The $LaPO_4$: Ce^{3+}, Nd^{3+} model system

In the $LaPO_4$: Ce^{3+}, Nd^{3+} system, Ce^{3+} is the donor and Nd^{3+} is the acceptor. Although the system is not commonly used for practical application, transfer from Ce^{3+} to Nd^{3+} has been described before in the literature [21]. The aim of studying luminescence decay curves of this system in this work is to study migration among Ce^{3+} centers. However, in order to analyze the decay curves in a quantitative manner, two other decay parameters should be studied first: the pure radiative decay rate of Ce^{3+} and the transfer rate from Ce^{3+} to Nd^{3+}. In order to measure the pure radiative decay rate of Ce^{3+}, it is useful to study luminescence decay of Ce^{3+} without other influences present. The decay should then be mono-exponential and the radiative decay rate can be determined by fitting the data to a mono-exponential function. The concentration of Ce^{3+} should be kept low in order to prevent migration over the ions and subsequent quenching on traps. A luminescence decay curve of $LaPO_4$: 0.1% Ce^{3+} was recorded by exciting at 270 nm and monitoring the luminescence intensity at 340 nm over time. The result can be seen in Fig. 4.11. As can be seen, the data correspond well to a mono-exponential decay. The data were fitted using the following mono-exponential function:

$$I(t) = I(0) * e^{-\gamma t} + b \tag{4.1}$$

Where $I(0)$ is the intensity at $t = 0$, b is the background intensity and γ is the radiative decay rate. The value for γ that yielded the best possible fit was 0.06002 ns^{-1}. The lifetime of the decay,

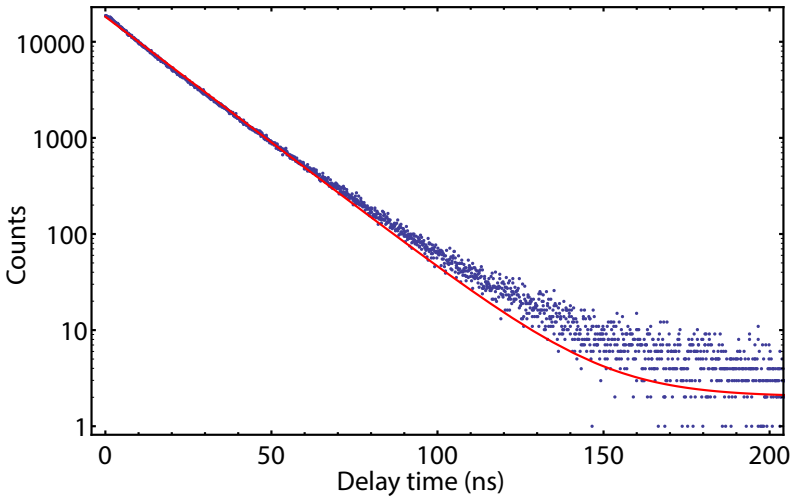

Figure 4.11: Decay curve of $LaPO_4$: 0.1% Ce^{3+}, with mono-exponential fit (red). Excitation wavelength was 270 nm, luminescence intensity was recorded at 340 nm.

defined as the inverse of the decay rate, is then 16.66 ns. The lifetime is short because the $5d \rightarrow 4f$ transition is parity allowed, causing relatively fast decay.

The second step is to add Nd^{3+} acceptors to the system in order to determine the rate of energy transfer from Ce^{3+} to Nd^{3+}. It is important to still keep the Ce^{3+} concentration low (0.1 %) to avoid migration over the Ce^{3+} ions for now. In order to obtain reliable results, samples with several Nd^{3+} concentrations were measured: 2.5%, 5%, 9% and 16.5% Nd^{3+}. The results are shown in Fig. 4.12. In order to make the comparison between the results more convenient, the curves were normalized, meaning that all data points were divided by the intensity at the start of the curve ($I(0)$). A single mono-exponential function (pure radiative rate) is also shown. The decay can never be slower than this mono-exponential function, because Ce^{3+} ions in the excited state always undergo radiative decay with decay rate γ.

We can see that at higher concentration of Nd^{3+}, the luminescence decays faster and becomes non-exponential. This is an expected result, because at higher acceptor concentration donor ions have more acceptor ions around them to which they can transfer the excitation energy. The non-exponential decay stems from the fact that ions are distributed randomly in the crystal and not all ions have the same amount of acceptor ions around them. The summation of several exponential functions with different decay rates results in a non-exponential decay.

In order to quantify the results and determine the rate of energy transfer from Ce^{3+} to Nd^{3+}, we have to fit to the more complicated equation (4.2). The derivation of this equation can be found in the Theory section.

$$I(t) = I(0) * e^{-\gamma t} \prod_{i}^{\text{shells}} (1 - \phi + \phi e^{-C_{\text{don}\rightarrow\text{acc}} t / r_i^6})^{n_i} + b \tag{4.2}$$

Here, γ is the pure radiative decay rate, ϕ is the fraction of cation sites occupied with acceptor ions, r_i is distance from the central donor and n_i is the amount of neighbors within the shell with radius r_i. A so-called 'neighbor list' has to be used with for each distance r_i the corresponding n_i.

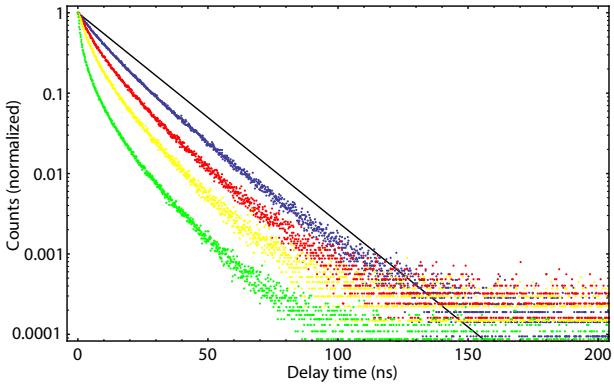

Figure 4.12: Decay curves of luminescence from $LaPO_4$: 0.1 % Ce^{3+} with varying Nd^{3+} concentrations: 2.5% (blue), 5% (red), 9% (yellow) and 16.5% (green). Excitation wavelength was 270 nm, luminescence intensity was recorded at 340 nm. A black line for pure radiative decay without background, with a decay rate of 0.06002 ns^{-1} is also shown.

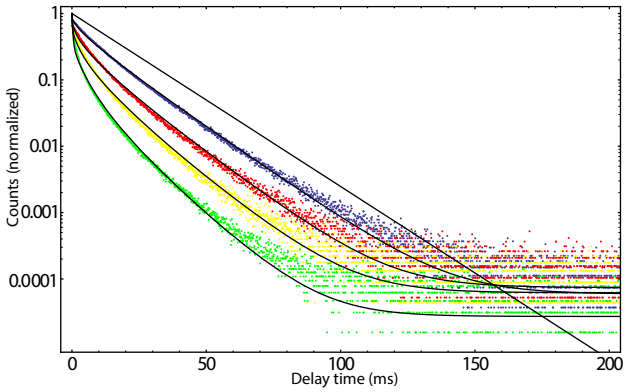

Figure 4.13: The same decay curves as in Fig. 4.12, with four different fit functions and a line for pure radiative decay without background, with a decay rate of 0.06 ns^{-1}

$C_{\text{don}\to\text{acc}}$ is a fitting parameter describing the strength strength between the donor and acceptor pair. This parameter is the "donor-acceptor strength" which was also described in the Theory section. It has dimensions of $s^{-1}m^6$. The data were fitted to equation (4.2), using different acceptor concentrations.

The result of the fitting procedure and calculated donor-acceptor strength values can be seen in Table 4.1. In the fitting procedure, the pure radiative decay rate was fixed at the value which was found with the $LaPO_4$: 0.1% Ce^{3+} sample: 0.06002 ns^{-1}, and the acceptor concentration was fixed at the calculated molar fractions. The background, amplitude $I(0)$ and the donor-acceptor strength were the fitting parameters. As can be seen, the fits correspond well with the data points, although the quality of the fits decreases with higher acceptor concentration. Therefore, for further analysis the Ce^{3+}–Nd^{3+} strength was estimated to be the average between the value for the 2.5% and 5% Nd^{3+}: around 0.0025 $ns^{-1}Å^6$. With this value and the value for the radiative rate, the

Molar fraction Nd^{3+}	Fit parameter Ce^{3+}– Nd^{3+} transfer strength (in $ns^{-1}Å^6$)
2.5%	0.00257
5%	0.00237
9%	0.00102
16.5%	0.00046

Table 4.1: The obtained fit parameter $C_{\text{don}\rightarrow\text{acc}}$ for Ce^{3+}– Nd^{3+} transfer, at different molar fractions of Nd^{3+} ions.

characteristic Förster distance for Ce^{3+}–Nd^{3+} can also be calculated, using equation (2.4). If we fill in the values ($C_{\text{don}\rightarrow\text{acc}} = 0.0025$ $ns^{-1}Å^6$ and $\gamma = 0.06002$ ns^{-1}) we obtain $R_0 = 0.59$ Å.

As a final step, the donor (Ce^{3+}) concentration was increased to study donor-to-donor migration. If this process occurs, the luminescence should decay more quickly at higher donor concentrations. Samples with a high concentration of Ce^{3+} were prepared and luminescence decay curves were measured. The result can be seen in Fig. 4.14.

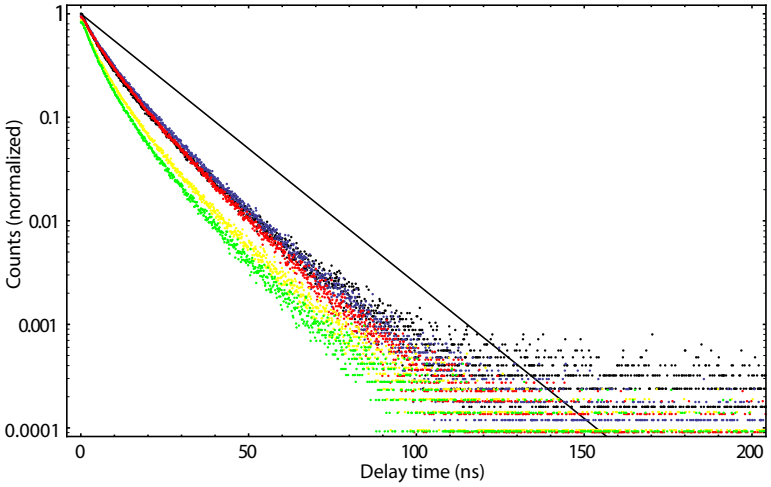

Figure 4.14: Decay curves of luminescence from $LaPO_4$: 5% Nd^{3+} with varying Ce^{3+} concentrations: 0.1% (black), 2.5% (blue), 5% (red), 9% (yellow) and 17% (green). A black line for pure radiative decay without background, with a decay rate of 0.06002 ns^{-1} is also shown.

The luminescence decays faster at higher Ce^{3+} concentration, although the effect is not very strong. The resulting decay curves were compared with a computer simulation (see section 4.4). The synthesized samples showed a slight yellow coloration, indicating the possible presence of Ce^{4+}. This coloration was also observed by van Schaik et al. [21]. They concluded that the Ce^{4+} did not replace lattice sites in the monazite structure, but was instead present as a second phase. This is in agreement with the results in Fig. 4.14. If Ce^{4+} were present in the monazite lattice, it would result in strong quenching of the luminescence, resulting in very fast decay. This is not what is observed. Nevertheless, the presence of Ce^{4+} can still be a problem, because it can still be present in the monazite lattice at low concentrations. Moreover, the exact concentration of Ce^{3+} is not known and likely to be somewhat lower than the value calculated from the amounts of rare earth oxides that were added.

4.3.2 The YPO_4: Gd^{3+}, Er^{3+} model system

Because $LaPO_4$: Ce^{3+}, Nd^{3+} possibly has the Ce^{4+} problem, energy migration was studied in other systems as well. Of these systems, the system YPO_4: Gd^{3+}, Er^{3+} has shown the most reliable results, and therefore we will show those here. In this system Gd^{3+} is the donor and Er^{3+} is the acceptor. Although the system is not often used for practical application, transfer from Gd^{3+} to Er^{3+} has been shown to occur in the literature [27]. It has to be noted that transitions on the Gd^{3+} ion can have a strong magnetic transition dipole moment as well as an electric transition dipole moment [28]. However, this is not expected to affect the luminescence dynamics, for the interaction between two magnetic dipoles also decreases with the sixth power of the distance. Therefore the procedure for studying energy migration was the same as for the previous system: first the radiative decay rate of the donor ion was measured, then energy transfer from a donor to an acceptor was studied by increasing the acceptor concentration gradually with a low concentration of donors, and finally donor-donor migration was studied by increasing the donor concentration and keeping the acceptor concentration constant.

The YPO_4: Gd^{3+}, Er^{3+} system was synthesized in two different ways: by solid state methods and by coprecipitation. Details can be found in the experimental section. In principle, coprecipitation should lead to more accurate results due to exclusion of transition metal ions. The oxalates of transition metal ions are much more soluble in water than the oxalates of lanthanide ions [29]; therefore only the lanthanide oxalates precipitate out of the solution while the transition metals remain in solution (and are subsequently removed). Additionally, the coprecipitation method is expected to yield more homogeneous samples because the precipitation of oxalates occurs in the liquid state which allows free motion of lanthanide ions.

Firstly, the radiative decay rate of Gd^{3+} was measured in YPO_4: 0.1% Gd^{3+} synthesized with the coprecipitation method. The Gd^{3+} ions were excited with a 272 nm laser pulse to the $^6P_{5/2}$ level. Rapid non-radiative decay causes the system to fall back quickly to the lower $^6P_{7/2}$ level. The luminescence decay of the emission from this level to the ground state (^8S) was then measured, at a wavelength of 308 nm. The result can be seen in Fig. 4.15. The lifetime of the Gd^{3+} emission was measured to be 4.454 ms. The lifetime is relatively long because the $f - f$ transition is parity forbidden, making direct radiative decay less probable.

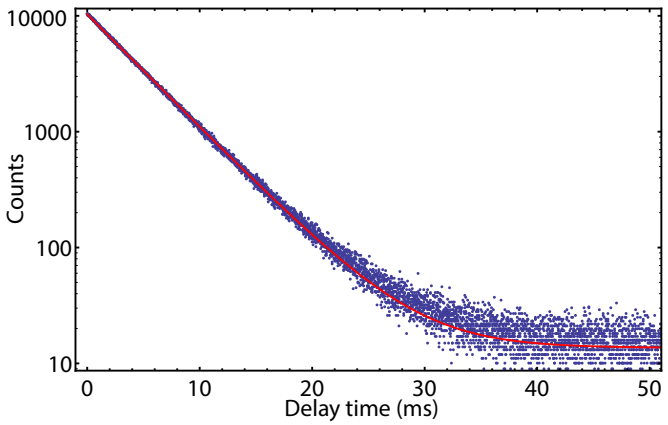

Figure 4.15: Decay curve of YPO_4: 0.1% Gd with mono-exponential fit (red). Excitation wavelength was 272 nm, luminescence intensity was recorded at 308 nm.

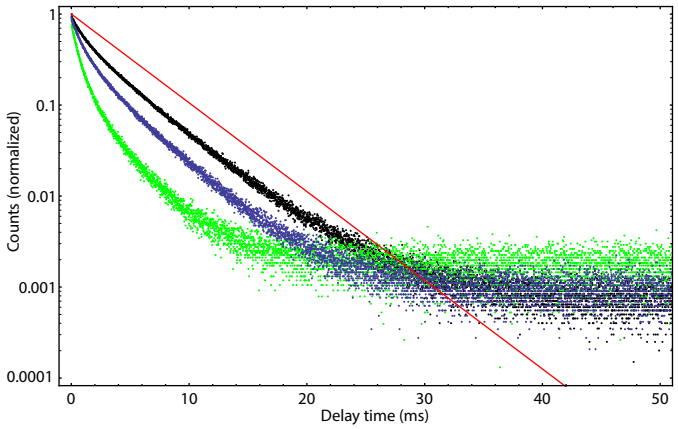

Figure 4.16: Decay curves of luminescence from YPO_4: 0.1% Gd^{3+} with increasing Er^{3+} concentrations: 5% (black), 10% (blue) and 20% (green). Synthesis was performed using the coprecipitation method. Excitation wavelength was 272 nm, luminescence intensity was recorded at 308 nm. A red line for pure radiative decay without background, with a decay rate of 0.2245 ms^{-1} is also shown.

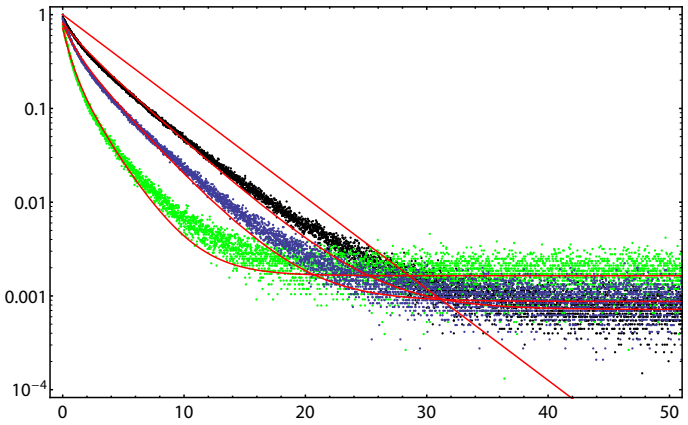

Figure 4.17: The same luminescence decay curves as in Fig. 4.16. An analytical expression (4.2) was used to fit the data and shown as red lines. The obtained fit parameters can be seen in Table 4.2. A red line for pure radiative decay without background, with a decay rate of 0.2245 ms^{-1} is also shown.

Next, the concentration of Er^{3+} was increased. In Fig. 4.16 and 4.17 the results can be seen. As expected, the luminescence decay accelerates at higher acceptor concentration. We can see in Table 4.2 that the Gd^{3+}– Er^{3+} strength is much lower than, for example, the Ce^{3+}– Nd^{3+} strength. The difference can be explained by the parity-forbidden nature of both the $f - f$ relaxation of Gd^{3+} and the $f - f$ excitation of Er^{3+}. In the event of a transfer between Ce^{3+} and Nd^{3+}, only the $f - f$ excitation of Nd^{3+} is forbidden. Additionally, the spectral overlap between Gd^{3+} excitation and emission may play a role; this is hard to tell because this spectral overlap cannot be measured

Molar fraction Er^{3+}	Fit parameter Gd^{3+}– Er^{3+} transfer strength (in $ms^{-1}Å^6$)
5%	0.00157
10%	0.00224
20%	0.00264

Table 4.2: The obtained fit parameter $C_{\mathrm{don}\to\mathrm{acc}}$ for Gd^{3+}– Er^{3+} transfer, at different molar fractions of Er^{3+} ions.

directly.

The system was also synthesized with the solid state method. The result can be seen in Fig. 4.18. The luminescence decay is much faster than for the samples synthesized with the coprecipitation method, and barely accelerates at higher acceptor concentration. Possibly, the existence of traps or impurities (e.g. transition metal ions) accelerates the decay. Because the amount of traps or impurities is not constant in each sample, the results are not very reliable, as opposed to the results from the co-precipitation method. Therefore a fitting procedure was only attempted for the co-precipitation decay curves.

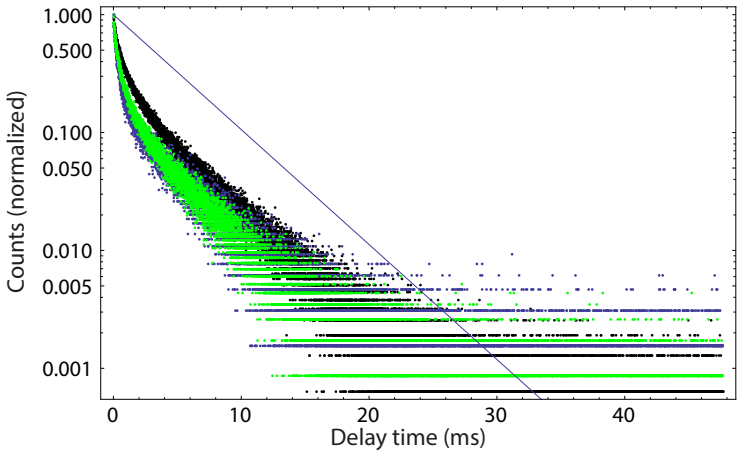

Figure 4.18: Decay curves of luminescence from YPO_4: 0.1% Gd^{3+} with varying Er^{3+} concentrations: 2.5% (black), 5% (blue) and 10% (green). Synthesis was performed using the solid state method. Excitation wavelength was 272 nm, luminescence intensity was recorded at 308 nm. A line for pure radiative decay without background, with a decay rate of 0.2245 ms^{-1} is also shown.

As previously described, the next step is to increase the donor (Gd^{3+}) concentration while keeping the acceptor concentration constant. It is expected that the luminescence decays even faster due to energy migration over donors and subsequent transfer to acceptors and traps.

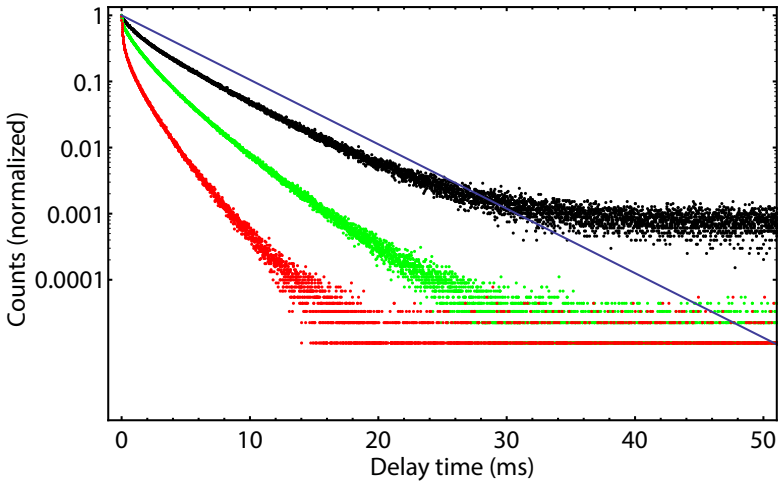

Figure 4.19: Decay curves of luminescence from YPO_4: 5% Er with varying Gd^{3+} concentrations: 0.1% (black), 5% (green) and 10% (red). Synthesis was performed using the coprecipitation method. Excitation wavelength was 272 nm, luminescence intensity was recorded at 308 nm. A blue line for pure radiative decay without background, with a decay rate of 0.2245 ms^{-1} is also shown.

The increase in donor concentration was attempted for both the solid state and coprecipitation samples. The result for the co-precipitation samples can be seen in Fig. 4.19. As can be seen, the luminescence decay accelerates rapidly at higher Gd^{3+} concentration. The results will be compared to a computer simulation (see section 4.4.2) but even qualitatively, the decay accelerates much faster than would be expected. For instance, in the theory section Fig. 2.6 shows only a small acceleration of the decay.

The increase in Gd^{3+} was also attempted for the samples synthesized with the solid state method. The result can be seen in Fig.4.20. As can be seen, the results are not very consistent: for instance, the blue graph (5% Gd^{3+}) already shows a faster decay than the red graph (10% Gd^{3+}). There is no reasonable explanation as to why this would occur. Possibly, there is a large amount of traps or defects present in the lattice, which complicates the decay curve analysis. For instance, if there is a large number of traps in a sample with low Gd^{3+} concentration, luminescence may actually decay faster than a sample with higher Gd^{3+} concentration but lower trap concentration.

The decay at short delay times is also faster than would be expected. This seems to point towards a fast-decaying component in the decay curve, which is consistent with the hypothesis that the trap concentration is high for the solid state samples. This fast decay is not as pronounced in the coprecipitation samples.

Overall, the data raises questions about the reproducibility of the measurements and synthesis, especially for the solid state samples.

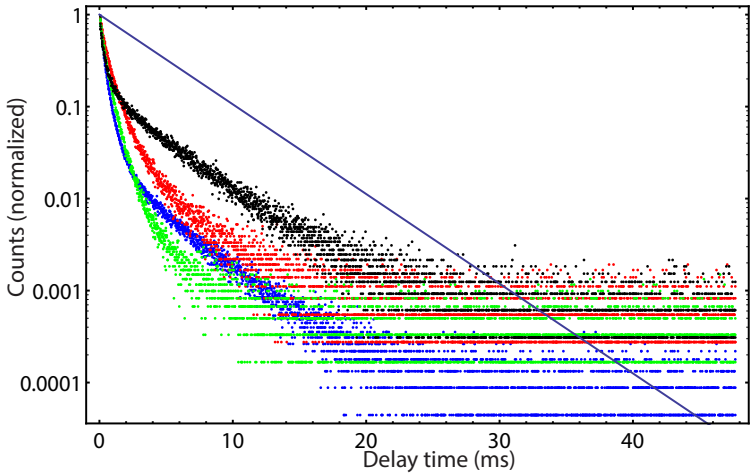

Figure 4.20: Decay curves of luminescence from YPO_4: 5% Er with varying Gd^{3+} concentrations: 0.1% (black), 5% (blue), 10% (red) and 20% (green). Synthesis was performed using the solid state method. Excitation wavelength was 272 nm, luminescence intensity was recorded at 308 nm. A line for pure radiative decay without background, with a decay rate of 0.2245 ms^{-1} is also shown.

4.4 Monte Carlo modeling and comparison with data

4.4.1 The $LaPO_4$: Ce^{3+}, Nd^{3+} model system

The $LaPO_4$: Ce^{3+}, Nd^{3+} system was modeled using Monte Carlo simulations. Details about the model can be found in section 2.4. The modeled decay curves can now be compared to the actual data. Ideally, this would make it possible to estimate the donor-to-donor migration strength and compare it to the donor-to-acceptor transfer strength. This comparison was only attempted for relatively low Ce^{3+} concentration: 5% Ce^{3+} and 9% Ce^{3+}. Luminescence decay curves of higher concentrations are probably less accurate due to the presence of Ce^{4+}.

In Fig. 4.21 a comparison between the model and the experimental data can be seen for 5% Ce^{3+} (left) and 9% Ce^{3+} (right). We can see that the effect of migration is almost negligible for 5% Ce^{3+} and more pronounced for 9% Ce^{3+}. Considering both graphs, we estimate a low value for the Ce^{3+}–Ce^{3+} strength: about 1/3 of the Ce^{3+}–Nd^{3+} strength. This corresponds to a strength of 0.0008 $ns^{-1}Å^6$. According to equation (2.4), the characteristic Förster radius R_0 for Ce^{3+}–Ce^{3+} is then 0.49 nm. This seems to indicate that the Ce^{3+}–Ce^{3+} migration process is quite slow; the reason could be that the spectral overlap between two Ce^{3+} centers is small.

We can also see that the Monte Carlo simulation does not exactly match the experimental data. The reason could be that the model assumes a completely random distribution of ions, whereas this is not necessarily the situation for a real crystal. Although crystallinity was optimized and the powders were mixed two times in a ball mill (see Experimental section), a completely random distribution cannot be guaranteed. The fact that the reaction was performed in the solid state (albeit at high temperatures) means that diffusion of ions during the reaction is slow. Therefore it is possible that some ions of the same element cluster together during the synthesis. If similar ions, e.g. Nd^{3+} ions cluster together, this will slow down the decay because it will be more difficult for the excitation energy to reach the Nd^{3+} centers.

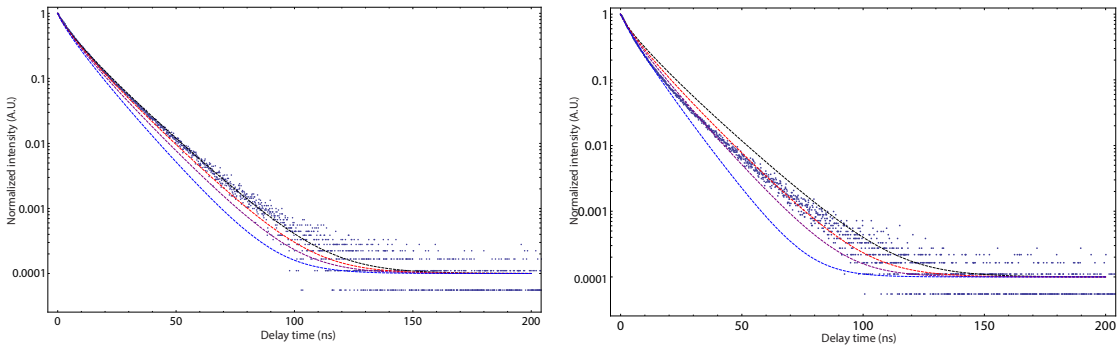

Figure 4.21: Comparison between luminescence decay curves of $LaPO_4$: 5% Ce^{3+}, 5% Nd^{3+} (left) and $LaPO_4$: 9% Ce^{3+}, 5% Nd^{3+} (right) and Monte Carlo computer simulations (dashed lines). For the simulations, four different Ce^{3+}–Ce^{3+} strengths were used: no migration (zero, black) one third of the Ce^{3+}–Nd^{3+} strength (red), equal to the Ce^{3+}–Nd^{3+} strength (purple), and three times as high as the Ce^{3+}–Nd^{3+} strength (blue).

Finally, the presence of Ce^{4+} (indicated by the yellow sample coloration) could be a factor in the disagreement between the model and the data. The presence of Ce^{4+} could have two effects: a faster quenching of the luminescence and a lower actual Ce^{3+} concentration. If the actual Ce^{3+} concentration is lower, for instance due to the formation of Ce^{4+} in a second phase, the effect of donor-to-donor migration is decreased because less Ce^{3+} centers are available for this process. This could cause a slower decay and thus an underestimation of the donor-to-donor migration strength.

4.4.2 The YPO_4: Gd^{3+}, Er^{3+} model system

Considering the problems described in the last paragraph, and the possible presence of Ce^{4+} we also attempted the study energy migration in another system: YPO_4: Gd^{3+}, Er^{3+}. This system has the advantage that both Gd^{3+} and Er^{3+} are very stable towards oxidation or reduction. Moreover, a coprecipitation synthesis can be used, which should lead to more homogeneous samples and the exclusion of possible transition metal ions.

We only compared Monte Carlo simulations with luminescence decay curves from coprecipitation samples, because these results were more consistent. In Fig. 4.22, the comparison with Monte Carlo simulations can be seen for the YPO_4: 5% Gd^{3+}, 5% Er^{3+} sample (left) and for the YPO_4: 10% Gd^{3+}, 5% Er^{3+} sample (right).

It can be seen that the model does not reproduce the experimental data well; especially for the YPO_4: 10% Gd^{3+}, 5% Er^{3+} there is a large discrepancy. The experimental data show a fast decay at the start of the curves that is not predicted by the model. Therefore it is questionable if this experimental curve is reliable.

For the YPO_4: 5% Gd^{3+}, 5% Er^{3+} it can be seen that the model corresponds best to the data if a Gd^{3+}–Er^{3+} strength of around 33x the strength of Gd^{3+}–Er^{3+} transfer is used; if the fast decaying component at the start of the curve is neglected, it reproduces the shape of the decay curve quite well. This corresponds to a strength of 0.08 $ms^{-1}Å^6$ for Gd^{3+}–Gd^{3+}. According to equation (2.4) this corresponds with a Förster radius $R_0 = 0.67$ nm for Gd^{3+}–Gd^{3+} migration. This means that the migration to a nearby Gd^{3+} ion is much more probable than transfer to an Er^{3+} ion at the same distance. A possible reason is that the spectral overlap of excitation and

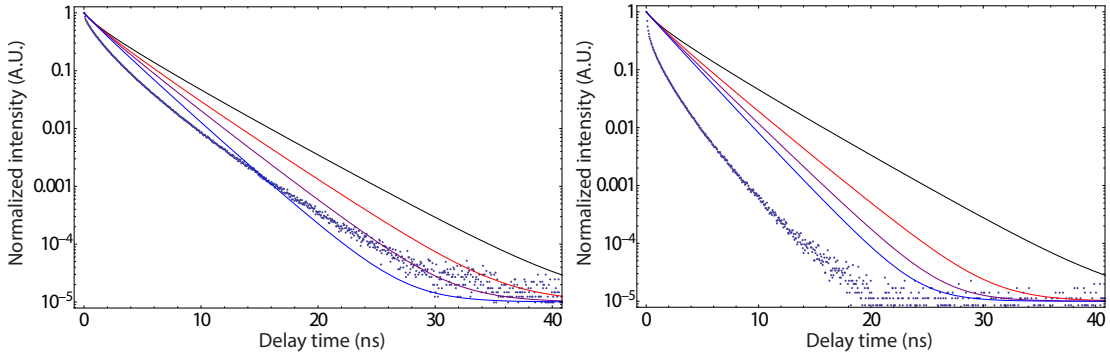

Figure 4.22: Comparison between luminescence decay curves of $LaPO_4$: 5% Gd^{3+}, 5% Er^{3+} (left) and $LaPO_4$: 10% Gd^{3+}, 5% Er^{3+} (right) and Monte Carlo computer simulations (dashed lines). For the simulations, four different Gd^{3+}–Gd^{3+} strengths were used: no migration (zero, black), ten times the Gd^{3+}–Er^{3+} strength (red), 33 times the Gd^{3+}–Er^{3+} strength (purple), and 100 times the Gd^{3+}–Er^{3+} strength (blue).

emission spectra between two Gd^{3+} centers could be very high.

A problem is that the model never corresponds completely with the data. At the start of the curves a faster component can be observed, which is not predicted by the model.

For the YPO_4: 10% Gd^{3+}, 5% Er^{3+} the correspondence of the data with the model is very weak; in the data a very fast decay is observed which is not predicted by the model.

There can be several reasons for the deviation between the model and the experimental data. Firstly, there could be traps or defects in the lattice that cause a faster quenching of the luminescence to take place. Secondly, other ions could be present that exhibit luminescence around the same wavelengths but decay with a faster rate; especially the presence of Ce^{3+}, which absorbs and emits around the same wavelengths, could be problematic. Thirdly, it is still possible that the samples are insufficiently homogeneous and clustering takes place; this could especially cause faster decay if Gd^{3+} ions cluster and the migration speed is fast. Lastly, the model assumes dipole-dipole interaction for the transfer and migration, leading to the sixth power distance dependence of the migration rates. This is not necessarily the case as quadrupole-dipole (eighth power dependence) or quadrupole-quadrupole (tenth power dependence) can also occur. According to Henderson and Imbusch [6] these processes can be important especially if the electric dipole moments are weak. The dipole moment of the Gd^{3+} emission transition is quite weak, considering the long lifetime of 4.45 ms; therefore these quadrupolar energy transfer processes could be a factor.

Chapter 5

Conclusion

In this research, the influence of donor-to-donor migration on luminescence was investigated, using lanthanide crystals doped with both donor and acceptor ions. Bulk powders of the materials $LaPO_4$: Ce^{3+}, Nd^{3+} and YPO_4: Gd^{3+}, Er^{3+} were synthesized using both a solid state ($LaPO_4$ and YPO_4) and coprecipitation method (YPO_4). X-ray diffraction was used to confirm the crystal structure of the compounds and to optimize the crystallinity. Luminescence properties of the materials was studied using emission and excitation spectra, and luminescence decay curves were measured using the TCSPC method.

Luminescence decay curves of samples with a low donor concentration were used to determine two essential parameters of the system: the radiative decay rate of the donor emission γ and the donor-acceptor transfer strength $C_{\text{don}\to\text{acc}}$. For $LaPO_4$: Ce^{3+}, Nd^{3+} these values were measured to be 0.06002 ns^{-1} for the radiative rate of Ce^{3+} and 0.0025 ns $^{-1}\text{Å}^6$ for the Ce^{3+}– Nd^{3+} transfer. For YPO_4: Gd^{3+}, Er^{3+} the radiative rate of Gd^{3+} was found to be 0.2245 ms^{-1} and the Gd^{3+}–Er^{3+} strength was found to be 0.00244 $\text{ms}^{-1}\text{Å}^6$.

Subsequently, luminescence decay curves of samples with a higher donor concentration were measured. A Monte Carlo simulation, based on differential equations describing the decay of a donor ion, was used to simulate decay curves of samples with a high donor concentration. A monazite ($LaPO_4$) or xenotime (YPO_4) crystal consisting of 1372 ions, with periodic boundary conditions, was simulated and donor and acceptor ions were placed randomly on the lattice. The rates of transfer and migrations between all ions were determined by using the obtained parameters for γ (radiative rate)and $C_{\text{don}\to\text{acc}}$ (transfer strength) and the distances between the ions involved. The parameter $C_{\text{don}\to\text{don}}$ (migration strength) was varied to obtain the best possible agreement with the experimental data.

The parameter $C_{\text{don}\to\text{don}}$ was estimated to be 0.0008 $\text{ns}^{-1}\text{Å}^6$ for Ce^{3+}–Ce^{3+} migration and 0.02 $\text{ms}^{-1}\text{Å}^6$ for Gd^{3+}–Gd^{3+}. The characteristic Förster radii were estimated to be $R_0 = 0.49$ nm for Ce^{3+}–Ce^{3+} and $R_0 = 0.67$ nm for Gd^{3+}–Gd^{3+}. The result for Ce^{3+}–Ce^{3+} is by far the most reliable. Some problems affecting the accuracy of the measurements were encountered for both systems; the $LaPO_4$: Ce^{3+}, Nd^{3+} system showed some evidence of the presence of Ce^{4+} albeit probably in a second phase. The YPO_4: Gd^{3+}, Er^{3+} showed poor agreement with the Monte Carlo at high Gd^{3+} concentrations, possibly due to distortions in the crystal lattice indicated by lower crystallinity. Clearly, more research is needed on possible improvements of the synthesis to obtain more reliable experimental results. However, this work provides a well working Monte Carlo model which can be used to make a useful comparison with the experimental data.

Chapter 6

Outlook

Based on the results obtained in this thesis, ideas for further research are:

- Improving the synthesis of luminescent phosphors. Although the phosphors described in this work have shown incorporation of the desired ions and good crystallinity, luminescent properties were sometimes lacking. In particular, the YPO_4: Gd^{3+}, Er^{3+} system lacked the expected Er^{3+} emission and the decay curves of the Gd^{3+} emission showed fast decay at the start of the curves. If the reason for this is the quenching of luminescence on traps or defects, this problem can possibly be alleviated, although traps can never be completely removed in a crystalline material [30]. The co-precipitation synthesis showed the best results, so it seems most logical to try to optimize this method. It is possible to try more heating stages, heat to higher temperature or add a flux to the reaction mixture. Progress could be measured by measuring the peak counts in the XRD spectrum. Additionally, it would be interesting to obtain more insight in the chemical and physical properties of the synthesized powders, for instance by measuring particle size with TEM or elemental composition with EDX.

- Making the fitting process more quantitative. In this work, only a qualitative attempt was made to fit the modeled decay curves to experimental data. This was in part because the experimental data are not completely reliable and obtaining a quantitative fit would not add much to the accuracy of the obtained migration strength. If the experimental data are made more reliable and reproducible, a quantitative fitting procedure could be constructed. The error between the modeled decay curve and the experimental data could be minimized using the migration strength $C_{don \rightarrow don}$ as the fit parameter. The migration strength could then be calculated with high accuracy.

- Extending the Monte Carlo model for upconversion and downconversion processes. If this can be done, an optimum concentration for an up- or downconverting phosphor can be calculated. Of the two, downconversion is by far the easiest to model. Recent attempts to model downconversion which takes place with the cooperative mechanism have shown promising results [31].

- Studying donor-to-donor migration in materials that are more relevant for up- or downconversion. An example of a system that has recently gained attention as downconversion material is YPO_4: Tb^{3+}, Yb^{3+} [2] [31]. Examples of materials that are interesting for upconversion processes are systems including Yb^{3+} and Er^{3+} ions [32] [33] [25]. This work has provided a

solid theoretical framework with which the influence of the migration process at high dopant concentrations can be estimated.

- Extending the work of this thesis by considering nanoparticles. The small size of nanocrystals can give rise to very interesting changes in properties such as different color, melting point, catalytic activity and so on [34]. Doped rare earth luminescent nanocrystals with a composition similar to the powders described in this work have been made recently [35]. The influence of simple energy transfer for these crystals has already been studied [12] [36]; extending this with donor-to-donor migration may be very interesting. For this purpose, the luminescence decay in a finite-sized nanocrystal could be modeled using a Monte Carlo simulation, and the resulting dynamics could be compared to experimental decay curves. However, surface defects are a well-known problem for nanocrystals [37] and this may complicate the analysis.

Chapter 7

Acknowledgments

This thesis would not have been possible without the help and support of several people. Firstly I would like to thank my daily supervisors, Mathijs de Jong and Freddy Rabouw. I have to say that it was a great luxury to have not one but two supervisors, of which both were equipped with an amazing amount of knowledge. Both of you were always willing to help me with synthesis, spectroscopy and Mathematica problems. With your daily dose of humor and sarcasm you were also very pleasant people to work with.

Secondly I would like to thank Andries Meijerink for supervision of this project. During our discussions, your great amount of knowledge always presented me with new ideas. Sometimes you were even willing to help with some technical problems, which was very nice, especially when you taught me that 'without duct tape one cannot do science'.

I would also like to thank Hans Ligthart for technical assistance (especially with the very dangerous 'ball mill') and Stephan Zevenhuizen for his help with computer-related problems.

Finally I would like to thank all students and staff members of the CMI group. It has been a very interesting, inspiring and fun 1.5 year. I especially liked the Sinterklaas and Christmas celebrations and klaverjas sessions during lunch breaks and it would not have been nearly as fun without all the group members. Thank you all!

Bibliography

[1] Th. Förster. Zwischenmolekulare Energiewanderung und Fluoreszenz. *Annalen der Physik*, 248(1938), 1939.

[2] P. Vergeer, T. Vlugt, M. Kox, M. den Hertog, J. van der Eerden, and A. Meijerink. Quantum cutting by cooperative energy transfer in $Yb_xY_{1-x}PO_4:Tb^{3+}$. *Physical Review B*, 71(1):014119, January 2005.

[3] J. T. Van Wijngaarden, S. Scheidelaar, T. J. H. Vlugt, M. F. Reid, and A. Meijerink. Energy transfer mechanism for downconversion in the (Pr^{3+}, Yb^{3+}) couple. *Physical Review B - Condensed Matter and Materials Physics*, 81(15):155112, April 2010.

[4] T.F. Schulze and T.W. Schmidt. Photochemical upconversion: Present status and prospects for its application to solar energy conversion. *Energy Environ. Sci.*, 8:103–125, March 1967.

[5] D.C. Yu, F.T. Rabouw, W.Q. Boon, T. Kieboom, S. Ye, Q.Y. Zhang, and A. Meijerink. Insights into the energy transfer mechanism in Ce^{3+}-Yb^{3+} codoped YAG phosphors. *Physical Review B*, 90:165126, 2014.

[6] B. Henderson and G. F. Imbusch. *Optical Spectroscopy of Inorganic Solids*. Oxford Science Publications, 1989.

[7] C.R. Varney, D.T. Mackay, A. Pratt, S.M. Reda, and F.A. Selim. Energy levels of exciton traps in yttrium aluminum garnet single crystals. *Journal of Applied Physics*, 111, 2011.

[8] M. Yokota and O. Tanimoto. Effects of Diffusion on Energy Transfer by Resonance. *Journal of the Physical Society of Japan*, 22:779–784, March 1967.

[9] A.I. Burshtein. Energy transfer kinetics in disordered systems. *Journal of Luminescence*, 34:167–188, November 1984.

[10] C. Carlsson, A. Larsson, M. Björkman, M. Jonsson, and B. Albinsson. Experimental and Simulated Fluorescence Depolarization Due to Energy Transfer as Tools to Study DNA-Dye Interactions. *Biopolymers*, 41:481–494, March 1996.

[11] J.K. Hannestad, P. Sandin, and B. Albinsson. Self-Assembled DNA Photonic Wire for Long-Range Energy Transfer. *Journal of American Chemical Society*, 130:1588915895, May 2006.

[12] F.T. Rabouw, S.A. den Hartog, T. Senden, and A. Meijerink. Photonic effects on the Förster resonance energy transfer efficiency. *Nature communications*, 5:3610, January 2014.

[13] C. E. Housecroft and Alan G. Sharpe. *Inorganic Chemistry, 3rd edition.* Pearson Education Limited, 2008.

[14] S.A. Cotton. *Scandium, Yttrium & the Lanthanides: Inorganic & Coordination Chemistry.* John Wiley & Sons, 2006.

[15] J.J. Markham. *Configurational Coordinates (Chapter in "Optical Properties of Solids").* Springer US, 1969.

[16] G.H. Dieke. *Spectra and energy levels of rare earth ions in crystals.* Interscience Press, 1968.

[17] P. Dorenbos. The $4f^n \leftrightarrow 4f^{n-1}5d$ transitions of the trivalent lanthanides in halogenides and chalcogenides. *Journal of luminescence*, 91:91–106, 2000.

[18] L. Aarts. *Downconversion for solar cells with lanthanide ion couples.* PhD thesis, Utrecht University, 2009.

[19] A.I. Burshtein. The influence of the migration mechanism of approaching particles on the energy transfer between them. *Journal of Luminescence*, 21:317–321, August 1979.

[20] Y. Ni and J.M. Hughes. Crystal chemistry of the monazite and xenotime structures. *American Mineralogist*, 80:21–26, 1995.

[21] W. Smit W. van Schaik, S. Lizzo and G. Blasse. Influence of Impurities on the Luminescence Quantum Efficiency of (La, Ce, Tb)PO_4. *Journal of the Electrochemical Society*, 140(1):216–222, 1993.

[22] G. Meyer. The ammonium chloride route to anhydrous rare earth chlorides- the example of YCl_3. *Inorganic Syntheses*, 25:146–150, 1989.

[23] P. Dorenbos. 5d-level energies of Ce3+ and the crystalline environment. III. Oxides containing ionic complexes. *Physical Review B*, 64(12):125117, September 2001.

[24] H. Meyssamy, K. Riwotzki, A. Kornowski, S. Naused, and M. Haase. Wet-Chemical Synthesis of Doped Colloidal Nanomaterials: Particles and Fibers of $LaPO_4$:Eu, $LaPO_4$:Ce, and $LaPO_4$:Ce,Tb. *Advanced Materials*, 11:840–844, 1999.

[25] A.S.S. de Camargo, L.A.O. Nunes, J.F. Silva, A.C. F. M. Costa, B.S. Barros, J.E.C. Silva, G.F. de Sa, and S. Alves. Efficient green and red upconversion emissions in Er^{3+}/Yb^{3+} co-doped $ZnAl_2O_4$ phosphor obtained by combustion reaction. *Journal of Physics: Condensed Matter*, 19:21–26, 2007.

[26] G. Lakshminarayana, E.M. Weis, A.C. Lira, U. Caldino, D.J. Williams, and M.P. Hehlen. Cross Relaxation in rare-earth-doped oxyfluoride glasses. *Journal of Physics: Condensed Matter*, 139:132–142, 2013.

[27] W. Van Schaik, S.H.M. Poort, J.J.H. Schlotter, E. Dorrestijn, and G. Blasse. Influence of Impurities on the Luminescence Quantum Efficiency of the Lamp Phosphor (Ce,Gd,Tb) MgB_5O_{10}. *Journal of the Electrochemical Society*, 141(8), 1994.

[28] C. M. Dodson and R. Zia. Magnetic dipole and electric quadrupole transitions in the trivalent lanthanide series: Calculated emission rates and oscillator strengths. *Physical Review B*, 86(12):125102, September 2012.

[29] C.E. Crouthamel and D.S. Martin. Solubility of the Rare Earth Oxalates and Complex Ion Formation in Oxalate Solution. II. Neodymium and Cerium(III). *Journal of the American Chemical Society*, 73:569–573, 1951.

[30] C. Kittel. *Introduction to Solid State Physics, 8th edition.* Wiley, 2005.

[31] F.T. Rabouw and A. Meijerink. Modeling the Cooperative Energy Transfer Dynamics of Quantum Cutting for Solar Cells. *Journal of Physical Chemistry C*, 119:2364–2370, 2015.

[32] G. Mialon, S. Türkcan, G. Dantelle, D.P Collins, M. Hadjipanayi, R.A. Taylor, T. Gacoin, A. Alexandrou, and J.P. Boilot. High Up-Conversion Efficiency of YVO_4:Yb,Er Nanoparticles in Water down to the Single-Particle Levels. *Journal of Physical Chemistry C*, 114:22449–22454, 2010.

[33] J. Feenstra, I.F. Six, M.A.H. Asselbergs, R.H. van Leest, J. de Wild, A. Meijerink, R.E.I. Schropp, A.E. Rowan, and J.J. Schermer. Er^{3+}/Yb^{3+} upconverters for InGaP solar cells under concentrated broadband illumination. *Physical Chemistry Chemical Physics*, 17:11234–11243, 2015.

[34] E. Roduner. *Size-dependent phenomena.* RSC Publishing, 2006.

[35] T. Senden. *Energy transfer and radiative decay properties of lanthanide doped $LaPO_4$ nanocrystals.* Master thesis, Utrecht University, 2006.

[36] T. Senden, F.T. Rabouw, and A. Meijerink. Photonic effects on the radiative decay rate and luminescence quantum yield of doped nanocrystals. *ACS Nano*, 9:1801–1808, 2015.

[37] L. Chen, P. Fleming, V. Morris, J.D. Holmes, and M. A. Morris. Size-Related Lattice Parameter Changes and Surface Defects in Ceria Nanocrystals. *Journal of Physical Chemistry C*, 114:12909–12919, 2010.